

1 **Title:** The influence of flow discharge variations on the morphodynamics of a  
2 diffluence-confluence unit on a large river.

3

4 **Corresponding Author:**

5 Christopher Hackney<sup>a</sup>

6

7 **Additional Authors:**

8 Stephen E. Darby<sup>b</sup>

9 Daniel R. Parsons<sup>a</sup>

10 Julian Leyland<sup>b</sup>

11 Rolf Aalto<sup>c</sup>

12 Andrew P. Nicholas<sup>c</sup>

13 James L. Best<sup>d</sup>

14

15 **Affiliations**

16 <sup>a</sup> Geography and Geology, School of Environmental Sciences, University of Hull, Hull,  
17 HU6 7RX, UK. E-Mail: C.Hackney@hull.ac.uk. Tel: 01482 465385

18 <sup>b</sup> Geography and Environment, University of Southampton, Highfield, Southampton,  
19 SO17 1BJ, UK.

20 <sup>c</sup> College of Life and Environmental Sciences, University of Exeter, Rennes Drive,  
21 Exeter, EX4 4RJ, UK.

22 <sup>d</sup> Departments of Geology, Geography and GIS, Mechanical Science and Engineering  
23 and Ven Te Chow Hydrosystems Laboratory, University of Illinois at Urbana-  
24 Champaign, 605 East Springfield Avenue, Champaign, IL 61820, USA.

25 **Abstract**

26 Bifurcations are key geomorphological nodes in anabranching and braided fluvial  
27 channels, and control local bed morphology, the routing of sediment and water, and  
28 ultimately define the stability of their associated diffluence-confluence unit. Recently,  
29 numerical modelling of bifurcations has focussed on the relationship between flow  
30 conditions and the partitioning of sediment between the bifurcate channels. Herein,  
31 we report on field observations spanning September 2013 to July 2014 of the three-  
32 dimensional flow structure, bed morphological change and partitioning of both flow  
33 discharge and suspended sediment through a large diffluence-confluence unit on the  
34 Mekong River, Cambodia, across a range of flow stages (from  $13,500 \text{ m}^3 \text{ s}^{-1}$  to  $27,000$   
35  $\text{m}^3 \text{ s}^{-1}$ ).

36

37 We show that the discharge asymmetry of the bifurcation varies with discharge and  
38 highlight that the influence of upstream curvature-induced water surface slope and  
39 bed morphological change may be first order controls in modulating the discharge  
40 asymmetry within the bifurcation. Analysis of discharge and sediment load throughout  
41 the diffluence-confluence unit reveals that during the highest ( $Q = 27,000 \text{ m}^3 \text{ s}^{-1}$ ), the  
42 downstream island complex is a net sink of sediment (losing  $2,600 \pm 2,000 \text{ kg s}^{-1}$   
43 between the diffluence and confluence), whereas during the rising limb ( $Q = 19,500$   
44  $\text{m}^3 \text{ s}^{-1}$ ) and falling limb flows ( $Q = 13,500 \text{ m}^3 \text{ s}^{-1}$ ) the sediment balance is in quasi-  
45 equilibrium. Comparison of our field data to existing bifurcation stability diagrams for  
46 bedload and suspended sediment load dominated bifurcations reveals that during  
47 lower (rising and falling limb) flow, the bifurcation is classified as unstable, yet  
48 transitions to a stable condition at high flows. However, over the long term (1959 –  
49 2013) aerial imagery reveals the diffluence-confluence unit to be fairly stable. We

50 propose, therefore, that the long term stability of the bifurcation, as well as the larger  
51 channel planform and morphology of the diffluence-confluence unit, is controlled by  
52 the dominant sediment transport regime of the system

53

54 **Key Words:** Bifurcation, Discharge, Large River, Suspended Sediment

## 55 **Introduction**

56 The passage of water and sediment through fluvial systems controls the evolution of  
57 channel planform, defines rates of channel adjustment and, over longer time scales,  
58 drives floodplain development and the construction of stratigraphy (Schumm, 1985;  
59 Aalto et al., 2003, 2008; Constantine et al., 2014). During its transit through the fluvial  
60 system, sediment may be stored in a range of in-channel landforms such as point or  
61 mid-channel bars, or during floods it can be deposited over bank onto islands and  
62 floodplains. Sediment may also be remobilised through bank erosion and the transfer  
63 of material from the floodplain into the channel. At larger spatial scales, it has been  
64 shown that channel planform attributes such as sinuosity and migration rate may be  
65 determined by sediment load and channel slope (Leopold and Wolman, 1957; Eaton  
66 et al., 2010; Constantine et al., 2014). However, the relationship between the rate at  
67 which sediment is supplied from the catchment upstream and the resulting imposed  
68 local channel morphology is spatially and temporally complex and it remains unclear  
69 how sediment dynamics through storage units modulate this larger-scale relationship.

70

71 The planform of large alluvial rivers has been observed to frequently tend towards an  
72 anabranching pattern (Latrubesse, 2008). Large rivers have also been shown to

73 possess some of the highest global sediment loads (Milliman and Syvitski, 1992), with  
74 the 30 largest rivers between them contributing ~20% of the global sediment flux  
75 transmitted to the ocean (Milliman and Farnsworth, 2011). Yet the passage of  
76 sediment and water through anabranching systems is complicated by the splitting and  
77 joining of the main channel around island and bar complexes (herein termed  
78 diffluence-confluence units). Diffluences, or bifurcations, are therefore key  
79 geomorphological nodes in anabranching channels, controlling local bed morphology,  
80 the routing of sediment and water, and ultimately defining the stability of diffluence-  
81 confluence units and channel planform (Bridge, 1993; Richardson and Thorne, 2001;  
82 Parsons et al., 2007; Hardy et al., 2011; Thomas et al., 2011; Szupiany et al., 2012;  
83 Kleinhans et al., 2013).

84

85 Recent numerical modelling of bifurcations has focussed on elucidating the  
86 relationship between flow conditions and the partitioning of sediment between  
87 bifurcate channels (Bolla Pittaluga et al., 2003; Kleinhans et al., 2008; Edmonds and  
88 Slingerland, 2008; Thomas et al., 2011; Marra et al., 2014). Much of this previous work  
89 has been concerned with coarse-grained bifurcating systems, with fine-grained  
90 systems receiving relatively less attention (Edmonds and Slingerland, 2008). This  
91 poses a problem when extrapolating bifurcation theory to the world's largest rivers  
92 which are mostly fine-grained systems, although Bolla Pittaluga et al. (2015) have  
93 proposed a unified theory of bifurcation stability which seeks to link sediment transport  
94 equations for both coarse and fine-grained bifurcations. Current models suggest that  
95 instability at a bifurcation may be initialised by positive feedback mechanisms  
96 associated with the distribution of water and sediment between two channels of  
97 unequal transport capacity (Bolla Pittaluga et al., 2003), emphasising the fundamental

98 importance of secondary flow fields in controlling the distribution of flow and, more  
99 importantly, sediment between each branch of the bifurcation (Kleinhans et al., 2008;  
100 Marra et al., 2014).

101

102 In contrast to theoretical studies, field studies have thus far revealed a lack, or reduced  
103 significance, of secondary flow structures at bifurcations in large (i.e., anabranching),  
104 alluvial, channels (McLelland et al., 1990; Parsons et al., 2007; Szupiany et al., 2009,  
105 2012). The apparent absence, or at least reduced significance, of secondary flow  
106 structures in such channels is likely due to the large width-to-depth ratios of natural  
107 (as opposed to their modelled cousins in flumes) large river channels, the associated  
108 reduction in cross-channel water surface slopes and the increasing role of form  
109 roughness, which acts to increase turbulence (Parsons et al., 2007). These  
110 observations raise questions as to the extent to which theories that invoke the  
111 significance of secondary flow structures in modulating the partitioning of sediment in  
112 large river bifurcations actually apply (Szupiany et al., 2012). Indeed, work by  
113 Szupiany et al. (2012) highlights other factors as being key to understanding the  
114 distribution of suspended sediments, and ultimately morphological changes, within a  
115 large river bifurcation. These characteristics, namely flow distribution, suspended  
116 sediment transport, bed shear stress and bed material grain size, will all vary to some  
117 degree as a function of varying flow discharge. However, no field studies have yet  
118 been conducted that examine the role of bifurcation dynamics across a range of flow  
119 discharges in large rivers, even though many such large rivers have highly seasonal  
120 flow regimes. It thus follows that, in order to better understand the stability and  
121 dynamics of large river bifurcations, and thus the morphodynamics of large river  
122 channel planforms, empirical studies that assess the distribution of water and

123 sediment flux through the discrete branches of diffidence-confluence units, and across  
124 a range of flow discharges, are required.

125

126 In this paper we report findings from a study into the partitioning of flow and suspended  
127 sediment at a bifurcation of a diffidence-confluence unit within a fine-grained,  
128 anabranching, reach of the Mekong River. Field surveys were conducted on the rising,  
129 flood and falling stages of the annual monsoonal flood pulse, providing new insight  
130 into the dynamics of a large river diffidence-confluence unit across a range (13,500 to  
131 27,000 m<sup>3</sup> s<sup>-1</sup>) of flow discharges. We detail the dynamics and structure of the variable  
132 flows within the bifurcation, before describing the morphodynamics of the bed at the  
133 upstream bifurcation and identifying local storages and sources of suspended  
134 sediment through the larger diffidence-confluence unit. This new field data set adds to  
135 the existing body of literature on large sand-bed river bifurcations within anabranching  
136 systems and, importantly, provides the first field-based contextualisation of the role  
137 that variations in flow discharge play in the distribution and dynamics of water and  
138 sediment within a large river diffidence-confluence unit.

139

## 140 **Study Site and Methodology**

### 141 *Study Site*

142 The Mekong River is one of the world's largest, ranking 12<sup>th</sup> in terms of its length  
143 (~4900 km) and 27<sup>th</sup> in terms of drainage area (816,000 km<sup>2</sup>; Kummu et al., 2008).  
144 The Mekong has an estimated mean annual sediment load of 87.4 ± 28.7 Mt yr<sup>-1</sup>  
145 (Darby et al., 2016) and mean annual runoff of 475 km<sup>3</sup> (MRC, 2009). The Mekong's

146 hydrology is dominated by single wet-season flow peaks associated with the passage  
147 of the East Asian and Indian monsoons (Adamson et al., 2009; Darby et al., 2013).  
148 The mean annual flow (1960 – 2002) at Kampong Cham, Cambodia, is  $14,500 \text{ m}^3 \text{ s}^{-1}$ ,  
149 but with an average flood discharge of  $52,500 \text{ m}^3 \text{ s}^{-1}$ . Upstream of the town of Kratie,  
150 Cambodia, the Mekong is largely controlled by bedrock (Gupta and Liew, 2007;  
151 Carling, 2009) such that its planform migration and channel geometry are highly  
152 constrained (Kummu et al., 2008; Hackney and Carling, 2011). South of Kratie, and  
153 upstream of the apex of its delta at Phnom Penh, expansive floodplains have  
154 developed allowing the unconstrained Mekong to migrate freely across largely  
155 Quaternary alluvium with characteristic anabranching and anastomosed channels  
156 developing (Carling, 2009). The area that is the focus of this study, comprising a large  
157 asymmetrical bar bifurcation (see Figure 1A), is located ~2 km south of the city of  
158 Kampong Cham, within the anabranching reach. Bed material was sampled using an  
159 Eckman grab-sampler at three locations evenly spaced across the channel at the head  
160 of the bifurcation (XS001) and during each survey period. The bed material in this  
161 reach was found to be predominantly fine to medium sand, but it coarsened during the  
162 higher flows observed in September 2013 ( $D_{50} = 0.4 \text{ mm}$  October 2013 and July 2014;  
163  $2 \text{ mm}$  September 2013).

164

165 **[INSERT FIGURE 1 HERE]**

166

167 Surveys of flow, river bed bathymetry and suspended sediment concentrations (see  
168 section below for details) were undertaken at three flow discharges corresponding to  
169 different stages of the annual flood pulse (Figure 1B): i) a 'rising limb' survey was

170 conducted in July 2014 when the discharge was  $19,500 \text{ m}^3 \text{ s}^{-1}$ ; ii) a 'peak flood' survey  
171 was conducted in September 2013 at a discharge of  $27,000 \text{ m}^3 \text{ s}^{-1}$  and iii) the 'falling  
172 limb' survey was undertaken at the end of October 2013, when flow discharge had  
173 reduced to  $13,500 \text{ m}^3 \text{ s}^{-1}$ .

174

### 175 *Bathymetric Surveys and Flow Mapping*

176 High-resolution MultiBeam Echo Sounding (MBES) surveys were conducted at the  
177 upstream bifurcation (see Figure 1A for location) to provide detailed bathymetry at the  
178 major bifurcation node. We employed a RESON SeaBat 7125 system operating at 400  
179 kHz and forming 512 equal angle beams across a 140-degree swath. A Leica 1230  
180 differential Global Positioning System (dGPS) was used to provide position with  
181 accuracies to  $\pm 0.02 \text{ m}$  and  $\pm 0.03 \text{ m}$  in the horizontal and vertical, respectively. The  
182 dGPS was coupled to an Applanix POS-MV WaveMaster Inertial Motion Unit (IMU)  
183 that also provided full, real-time, 3-D motion and heading data correction for the MBES,  
184 along with synchronisation of all survey data streams using the dGPS time stamp and  
185 a pulse per second (PPS) signal. Post-survey calibration and correction for angular  
186 offsets and the application of sound velocity corrections were applied to the MBES  
187 data within CARIS-HIPS (v.9) software.

188

189 Detailed three-dimensional time-mean flow velocity fields were obtained around the  
190 diffuence-confluence unit using a series of acoustic Doppler current profilers (aDcp).  
191 Due to instrument availability and the flow conditions at the time of the survey we  
192 employed two RDI Teledyne RioGrande 600 kHz and one RDI Teledyne RioGrande  
193 1200 kHz units. Flow measurements were made at a series of predetermined cross-



194 sections (Figure 1B). At each cross-section, multiple repeat surveys were undertaken  
195 to resolve the time-averaged flow field (Szupiany et al. 2007). At major cross-sections  
196 where analysis of the 3-D flow structures was undertaken, four passes were obtained  
197 (XS001 and XS007; Figure 1). At all other transects, where only discharge and  
198 suspended sediment flux was calculated, two passes per cross-section were made.  
199 Each aDcp unit was coupled to the same RTK dGPS used in the MBES surveys to  
200 determine the position and velocity of the survey vessel. Following Szupiany et al.  
201 (2007), boat speed and trajectory were constantly monitored during the survey to  
202 reduce associated errors. The primary and secondary flow structures (if present) at  
203 each cross-section were processed using the Velocity Mapping Toolbox (VMT;  
204 Parsons et al., 2013) and were defined using a zero net cross-stream discharge  
205 decomposition (Lane et al., 2000).

206

### 207 *Suspended Sediment Concentration and Suspended Sediment Flux*

208 Previous work has shown that suspended sediment concentration as measured at-a-  
209 point in a cross-section can be estimated using the corrected acoustic backscatter  
210 value recorded by the aDcp at the same location (Kostaschuk et al., 2005; Szupiany  
211 et al., 2009; Shugar et al., 2010). This relationship is based on the assumption that the  
212 intensity of the acoustic backscatter recorded by the aDcp is a function of not only  
213 equipment characteristics, but also water column conditions (i.e., the concentration  
214 and size of suspended sediment therein). Therefore, for a given instrument and for a  
215 given sediment type and sediment size distribution, a simple relationship between  
216 acoustic backscatter and sediment concentration should be obtainable (Szupiany et  
217 al., 2009).

218

219 Following Szupiany et al. (2009), we corrected the echo intensity values recorded by  
220 the aDcp using the simplified sonar equation:

$$221 \quad EL = SL + 10\log_{10}(PL) - 20\log_{10}(R) - 2\alpha_s R + S_v + RS \quad (1)$$

222 where  $EL$  is the signal intensity recorded by the aDcp,  $PL$ ,  $SL$  and  $RS$  are determined  
223 solely by the individual instrument characteristics,  $R$  is the distance between the aDcp  
224 transducer and the measured volume,  $\alpha_s$  is the sound absorption coefficient, and  $S_v$  is  
225 the volume scattering strength. To provide a measure of suspended sediment  
226 concentrations with which to regress the recorded acoustic backscatter signal, we  
227 collected point samples using a three litre Van Dorn (Rutner) sampler at three evenly  
228 spaced verticals across the channel and at three points within each vertical profile.  
229 These point samples were obtained across a variety of flow conditions and locations  
230 such that we were able to produce unique calibration curves specific to each of the  
231 three aDcp units employed in this study (Figure 2). The range of suspended sediment  
232 concentrations covered by the sampling procedure was 6 to 531 mg L<sup>-1</sup>. Simultaneous  
233 aDcp measurements were taken to enable direct comparison between the directly  
234 measured suspended sediment concentrations and the recorded acoustic backscatter.  
235 The resultant calibration curves (Figure 2) display high correlations that are significant  
236 at 95% confidence levels (with  $R^2$  values of 0.83, 0.87 and 0.67, for the two 600 kHz  
237 units and the 1200 kHz unit, respectively). Using these relationships, along with the  
238 flow velocity field across each aDcp survey transect, we then estimated fluxes of  
239 suspended sediment at each location. Specifically, for each cross-section transect, the  
240 acoustic backscatter values were converted to a suspended sediment concentration  
241 using the appropriate calibration curve. The associated velocity measurements from

242 the aDcp were then used to convert these concentrations into a mass flux at each cell,  
243 and finally these were integrated out across each cross-section to provide an  
244 instantaneous section-averaged suspended sediment load ( $\text{kg s}^{-1}$ ).

245

246 **[INSERT FIGURE 2 HERE]**

247

## 248 **Bifurcation dynamics**

249 To understand the role that flow discharge variations play on the functioning of a large  
250 river bifurcation and the effects of such variations on the diffluence-confluence unit  
251 downstream of the bifurcation, we first report the hydrodynamic, sediment transport  
252 and morphological variability observed at the bifurcation apex across the three  
253 observed flow discharges. We then discuss how the partitioning of water and  
254 suspended sediment through the diffluence-confluence unit varies as a function of flow  
255 discharge.

256

257

### 258 *Hydrodynamics of a large river bifurcation*

259 Figure 3 displays the primary flow velocities (coloured map) and secondary flow  
260 vectors (zero net cross-stream discharge decomposition; arrows) derived from the  
261 aDcp surveys conducted at XS001 (Figure 1A), the transect located at the bifurcation  
262 head, during each of the three field surveys. During the rising limb (July 2014,  $Q =$   
263  $19,500 \text{ m}^3 \text{ s}^{-1}$ ), the depth-averaged cross-sectional velocity ( $U$ ) was  $0.98 \text{ m s}^{-1}$ , during

264 the highest discharges (September 2013,  $Q = 27,000 \text{ m}^3 \text{ s}^{-1}$ )  $U = 1.14 \text{ m s}^{-1}$ , whereas  
265 during the falling limb (October 2013,  $Q = 13,500 \text{ m}^3 \text{ s}^{-1}$ )  $U = 0.7 \text{ m s}^{-1}$ . As can be seen  
266 in Figure 3, during the rising and falling limbs of the flood wave, the high-velocity core  
267 is confined within the centre of the channel, with downstream flow velocities  
268 decreasing towards either bank. On the rising limb (July 2014) the high velocity core  
269 (defined as the area of flow where the ratio of observed flow to mean cross-section  
270 flow is greater than or equal to 1.5) comprises only 3% of the total area of the channel.  
271 During the falling limb (October 2013) the high velocity core comprises 10% of the  
272 channel, whereas during the high discharge event of September 2013, the high-  
273 velocity core occupies 8% of the channel cross-sectional area. Although flow velocity  
274 decreases towards the banks, during September 2013, flows of  $1.2 \text{ m s}^{-1}$  and greater  
275 are found within approximately 200 m from the banks. During the falling limb (October  
276 2013), such velocities are found only in the high-velocity core, approximately 500 m  
277 from the banks (Figure 3). At higher flows, there is less variation in high velocities  
278 across the channel, making it less likely for spatial variations in suspended sediment  
279 concentration to occur within the channel cross-section.

280

281 **[INSERT FIGURE 3 HERE]**

282

283 The secondary flow velocity vectors plotted on Figure 3 also reveal that, during all  
284 three surveys, flow is directed outwards from the centre of the channel towards both  
285 banks. Figure 3 also shows that there is little to no exchange of flow in the vertical at  
286 these flow stages. That is to say, flow is predominantly being steered laterally to the  
287 left and right banks, and thus down the left and right hand channels of the bifurcation,

288 without forming secondary flow cells. This is not surprising given that fully defined  
289 helical, secondary flow may be caused by either the interactions between centrifugal  
290 and pressure gradient forces or the heterogeneity and anisotropy of turbulence  
291 (Parsons et al., 2007). In large rivers, the large width:depth ratios tend to reduce the  
292 influence of cross-stream water surface slopes, dampening the development of  
293 secondary flow cells. It is clear, however, that the location of the shear layer marking  
294 the divergence in flow shifts across the channel with changing flow discharge. During  
295 the rising limb (July 2014) the divergence occurs ~500 m from the left hand bank.  
296 During high flows (September 2013) the divergence occurs ~ 725 m from the left and  
297 bank, whilst during the falling limb (October 2013) the secondary flow diverges ~520  
298 m from the left hand bank. This implies that during higher flows, the flow field at the  
299 diffluence becomes more asymmetrical with greater volumes of water being directed  
300 down the left hand channel of the bifurcation (this is discussed further below).

301

302 Analysis of the cross-stream water surface elevations (recorded on average at a ~2.5  
303 m spacing across the channel width) derived from the dGPS elevations recorded whilst  
304 conducting the MBES surveys during the different flow discharges (Figure 4A and B)  
305 reveals that, during the highest discharges (September 2013), the mean cross-stream  
306 water surface slope, calculated as the difference between the water surface elevations  
307 at the left and right hand bank divided by the cross-stream distance, is  $8 \times 10^{-5} \text{ m m}^{-1}$ ,  
308 reducing to  $3 \times 10^{-5} \text{ m m}^{-1}$  during the falling limb (October 2013), with a similar value of  
309  $4 \times 10^{-5} \text{ m m}^{-1}$  observed during the rising limb (July 2014) flow. It is noted here that the  
310 highest water surface elevations reported in Figure 4 are on the left hand bank. The  
311 planform of the main channel upstream of the survey area is that of a left turning bend,  
312 such that the highest water surface elevations may be expected to be found on the

313 outer, right hand bend. However, the presence of a constriction in the main channel  
314 ~1.2 km upstream of the survey location evidently deflects the high velocity core  
315 towards the left hand bank. This is visible in the MBES data reported in Figure 5, where  
316 the greatest depths are seen towards the left hand bank. This topographic flow  
317 steering explains how flow is forced towards the left hand bank, raising water surface  
318 elevations there, and likely plays a key role in conditioning the hydrodynamics at this  
319 bifurcation. As can be seen in Figure 4A, the strength and effect of this steering is  
320 reduced during lower flows. The impact of upstream curvature on discharge  
321 partitioning at bifurcations has long been recognised (Kleinhans et al., 2008; Thomas  
322 et al., 2012; Marra et al., 2013), with lower cross-stream water surface slopes (i.e. less  
323 water being forced towards one bank or another) resulting in a more even distribution  
324 of flow within the channel.

325

326 **[INSERT FIGURE 4 HERE]**

327

328 In addition to the role of cross-stream water surface slope, both inertial effects and  
329 secondary flow have previously been shown to control discharge partitioning at  
330 bifurcations in large rivers (Parsons et al., 2007; Szupiany et al., 2012). Accordingly,  
331 for each of the surveys conducted here, we defined the dimensionless strength of the  
332 secondary flow component relative to the primary flow velocity,  $U_{s*}$ , following  
333 Blanckaert (2009):

334 
$$U_{s*} = \sqrt{\langle (v_n - u_n)^2 \rangle} / U \quad (2)$$

335 where  $(v_n - u_n)$  is the depth-averaged transverse velocity component of the curvature  
336 induced secondary flow and  $U$  is the depth-averaged velocity. Using Eq. 2, when the  
337 cross-stream water surface slope is at its lowest ( $3 \times 10^{-5} \text{ m m}^{-1}$ ; October 2013,  $Q =$   
338  $13,500 \text{ m}^3 \text{ s}^{-1}$ ), the secondary flow strength is estimated to have a value of  $U_{s*} = 0.06$ .  
339 At the highest cross-stream water surface slope ( $8 \times 10^{-5} \text{ m m}^{-1}$ ; September 2013,  $Q =$   
340  $27,000 \text{ m}^3 \text{ s}^{-1}$ ), the estimated value of  $U_{s*}$  decreased to 0.03, whereas it rose again to  
341 a value of 0.04 during July 2014 ( $Q = 19,500 \text{ m}^3 \text{ s}^{-1}$ ), when the cross-stream water  
342 surface slope was  $4 \times 10^{-5} \text{ m m}^{-1}$ . These data show that the observed increase in depth-  
343 averaged primary flow velocities is proportionally greater than the secondary flow  
344 component as the flow discharge increases. It is therefore likely that inertial effects  
345 have a greater effect on the distribution of water and sediment at this bifurcation during  
346 lower discharges, when the secondary flow is relatively stronger. Conversely, at the  
347 peak flow discharge, it appears that upstream, curvature-induced, forcing is the main  
348 control on water and sediment distribution through the bifurcation (discussed further  
349 below).

350

351 The above reported variations in flow velocity, cross-stream water surface elevation  
352 and secondary flow strength impact upon the boundary shear stress,  $\tau_b$ , which in turn  
353 affects bed material transport capacity. Here, we estimate boundary shear stress using  
354 the Manning-Strickler law of bed resistance:

$$355 \quad \tau_b = \rho C_f U^2 \quad (3)$$

356 where  $\rho$  is the fluid density, and  $C_f$  is the coefficient of friction computed using:

$$357 \quad C_f = \left[ \alpha_r \left( \frac{H}{k_s} \right)^{1/6} \right]^{-2} \quad (4)$$

358 where  $H$  is the mean flow depth,  $\alpha_r$  is set as 8.1 (Parker, 1991), and  $k_s$  is equal to  
359  $2.95D_{84}$  (here  $D_{84} = 2.7$  mm in September 2013 and 0.5 mm in October 2013 and July  
360 2014) as specified by Whiting and Dietrich (1990). Equation 3 can be generalised as  
361 a two-dimensional vector with streamwise ( $\tau_{bu}$ ) and cross-stream ( $\tau_{bv}$ ) component  
362 magnitudes of:

$$\begin{aligned} \tau_{bu} &= \rho C_f U \sqrt{U^2 + V^2} \\ \tau_{bv} &= \rho C_f V \sqrt{U^2 + V^2} \end{aligned} \quad (5)$$

364 where  $V$  is the depth-averaged cross-stream velocity following Engel and Rhoads  
365 (2016).

366

367 As can be seen in Figure 4B, bed shear stresses increase towards the centre of the  
368 channel during all three surveys, with the peaks in boundary shear corresponding to  
369 the locations of the high velocity cores shown in Figure 3. Greater values of  $\tau_{bu}$  are  
370 experienced during the higher flow conditions in September 2013 ( $Q = 27,000 \text{ m}^3 \text{ s}^{-1}$ ),  
371 where values reach a maximum of  $1.5 \text{ N m}^{-2}$  in the centre of the channel, decreasing  
372 rapidly towards the channel margins. By comparison, the peak boundary shear stress  
373 during October 2013 ( $Q = 13,500 \text{ m}^3 \text{ s}^{-1}$ ) is  $0.6 \text{ N m}^{-2}$  and the variation across the  
374 channel is much more subdued, with a gradual decline towards the margins. During  
375 July 2014 ( $Q = 19,500 \text{ m}^3 \text{ s}^{-1}$ ), the peak  $\tau_{bu}$  was  $1.4 \text{ N m}^{-2}$  but fairly high  $\tau_{bu}$  values of  
376  $\sim 0.5 \text{ N m}^{-2}$  persist to within 200 m of the channel banks. Thus, despite their lower  
377 magnitudes, the distribution of bed shear stresses is much more even across the  
378 channel during the rising and falling limbs of the flood than during the highest flow  
379 discharge observed in this study.

380



381 By examining the cross-stream component of the bed shear stress, we are able to  
382 infer the potential direction of bedload transport at the apex of the bifurcation given the  
383 sign of  $\tau_{bv}$ . Positive  $\tau_{bv}$  indicates shear stresses directed towards the left bank,  
384 whereas negative  $\tau_{bv}$  values indicate shear stresses directed towards the right bank.  
385 Figure 4C shows that the highest magnitudes of  $\tau_{bv}$  occur during the highest  
386 discharges in September 2013 ( $Q = 27,000 \text{ m}^3 \text{ s}^{-1}$ ), with the lowest magnitudes of  $\tau_{bv}$   
387 during October 2013 ( $Q = 13,500 \text{ m}^3 \text{ s}^{-1}$ ). In the centre of the channel, between 400 to  
388 700 m from the left hand bank, the magnitude of  $\tau_{bv}$  is negligible across all three  
389 surveys. Consequently, during all the flow discharges observed here, bed shear stress  
390 is directed predominantly in the downstream direction in the central portion of the  
391 channel. However, in a zone located at a distance of between 0 to 400 m from the left  
392 hand bank, bed shear stress is clearly directed towards the left hand bank during the  
393 high ( $\tau_{bv} = 0.28 \text{ N m}^{-2}$ ; September 2013,  $Q = 27,000 \text{ m}^3 \text{ s}^{-1}$ ) and rising limb ( $\tau_{bv} = 0.16$   
394  $\text{N m}^{-2}$ ; July 2014,  $Q = 19,500 \text{ m}^3 \text{ s}^{-1}$ ) flows, whereas during the falling limb flow there  
395 is a negligible cross-stream component of boundary shear stress. Conversely, in the  
396 zone located from 700 m to 1100 m from the left bank, boundary shear stress is  
397 directed toward the right hand bank. Magnitudes of  $-0.3 \text{ N m}^{-2}$  (where the negative  
398 sign defines the shear stress being directed from left to right) during the September  
399 2013 high flow and  $-0.22 \text{ N m}^{-2}$  during the July 2014 rising limb flow, indicate that the  
400 magnitude of boundary shear stress directed towards the right bank is greater than  
401 the boundary shear directed towards the left bank during the same flows. Even during  
402 the falling limb, the highest positive  $\tau_{bv}$  magnitude observed ( $0.08 \text{ N m}^{-2}$ ) is smaller  
403 than the highest negative  $\tau_{bv}$  magnitude observed ( $-0.15 \text{ N m}^{-2}$ ). This implies that the  
404 greatest sediment transport capacities are located within the right hand portion of the  
405 channel.

406

407 *Bed morphodynamics of a large river bifurcation*

408 It has been shown in previous research that deposition and erosion in bifurcate  
409 channels impact upon the transverse bed slope that may steer discharge and  
410 sediment down the deeper, dominant channel (Bolla Pittaluga et al., 2003; Kleinhans  
411 et al., 2008; Marra et al., 2013). Over the three surveys conducted in this study,  
412 morphological changes of the bed were revealed through MBES surveys of the  
413 bifurcation. As can be seen in Figure 5, these MBES surveys reveal net deposition of  
414 the bed of up to 8 m in places over the period October 2013 to July 2014. The areas  
415 of greatest deposition occur at the margins of the channel. It is in these areas that bed  
416 shear stresses are at their lowest (Figure 4B). In the central section of the channel,  
417 there is little (<1 m) deposition, which can be explained by bedform migration and  
418 translation during this period rather than systematic sediment accumulation on the bed.  
419 It is in this section where bed shear stresses have been shown to be at their greatest  
420 (Figure 4B). The absence of erosion here implies that there is sufficient incoming  
421 sediment transported as bedload through this reach to maintain the bed topography  
422 at the upstream extent of the bifurcation throughout the period monitored.

423

424 **[INSERT FIGURE 5 HERE]**

425

426 **Implications for the diffuence-confluence unit**

427 A network of aDcp surveys through the branches of the diffuence-confluence unit  
428 downstream of the bifurcation (Figure 1A) allows examination of the role that flow

429 discharge variations plays in controlling the hydrodynamics and morphodynamics of a  
430 large river bifurcation and, in particular, the effect this has in defining the partitioning  
431 of flow discharge and suspended sediment around the downstream island complex.  
432 Such analysis is important because the flows of sediment and water around the island  
433 complex define the mobility of the island and thus impact upon the stability of the  
434 bifurcation and overall channel planform. Henceforth, the left (main) channel of the  
435 bifurcation will be termed C<sub>1</sub> whilst the right (subsidiary) channel will be termed C<sub>2</sub>.

436

437 On the rising limb of the monsoon flood (July 2014;  $Q = 19,500 \text{ m}^3 \text{ s}^{-1}$ ), there was a  
438 net loss of  $500 \text{ m}^3 \text{ s}^{-1} \pm 3850 \text{ m}^3 \text{ s}^{-1}$  (~3% of the total discharge; where the error  
439 estimate quoted equates to the summed errors of the water flux estimated at XS001  
440 and XS007) between the apex of the bifurcation and the downstream confluence  
441 (Figure 6). This transmission loss lies within the error associated with the discharge  
442 estimates derived from aDcp units, here defined as one standard deviation of the  
443 individual discharge estimates of the four repeat transects taken at XS001 during all  
444 three surveys. Note that this one standard deviation estimate equates to roughly 10%  
445 of the combined discharge estimate, which is somewhat higher than previous  
446 estimates of aDcp error (5%; Meuller and Wagner, 2009). At high flows (September  
447 2013;  $Q = 27,000 \text{ m}^3 \text{ s}^{-1}$ ), a net transmission loss of  $1,500 \text{ m}^3 \text{ s}^{-1} \pm 5250 \text{ m}^3 \text{ s}^{-1}$  was  
448 observed between the upstream bifurcation and downstream confluence (Figure 6 c  
449 and d). This loss (~6%) is greater than that during the rising stage and, however still  
450 falls between the summative errors to XS001 and XS007 and so can be said to be in  
451 balance. Within the individual links of the bifurcation unit, the biggest loss of discharge  
452 can be identified as occurring between XS002 and XS003A in C<sub>1</sub>, with a net loss of  
453  $3,500 \text{ m}^3 \text{ s}^{-1} \pm 3,750 \text{ m}^3 \text{ s}^{-1}$  (Figure 6 d). Analysis of levee heights extracted from the

454 Shuttle Radar Topography Mission (SRTM) 90 m spatial resolution elevation data  
455 around the outer banks of C<sub>1</sub> and C<sub>2</sub> reveals that at this flow stage water levels  
456 (measured at 14 m above Ha Tien datum at Kampong Cham) begin to overtop the  
457 levee crests down C<sub>1</sub>, resulting in a transfer of water from the main channel onto the  
458 floodplain; accounting for the loss of water seen in this link. Immediately below this  
459 link is an off-take channel through which a further  $500 \text{ m}^3 \text{ s}^{-1} \pm 50 \text{ m}^3 \text{ s}^{-1}$  (based on  
460 direct aDcp survey) is lost.

461

462 **[INSERT FIGURE 6 HERE]**

463

464 During the falling limb of the hydrograph (October 2013;  $Q = 13,500 \text{ m}^3 \text{ s}^{-1}$ ), a net gain  
465 of  $2,500 \text{ m}^3 \text{ s}^{-1} \pm 2,950 \text{ m}^3 \text{ s}^{-1}$  is apparent between the head and tail of the island  
466 complex (Figure 6 e and f). The greatest influx of flow discharge occurs towards the  
467 end of the reach around the confluence zone, where C<sub>1</sub> and C<sub>2</sub> re-join just upstream  
468 of XS007. Here an additional  $2,700 \text{ m}^3 \text{ s}^{-1} \pm 2930 \text{ m}^3 \text{ s}^{-1}$  was recorded by the aDcp.  
469 Satellite imagery from the approximate date of this survey (Landsat 8 October 2013  
470 Julian day 297) reveals there is a large store of water present on the floodplain in close  
471 proximity to this region (see region of water on floodplain south of XS006 shown on  
472 Figure 1A). It is therefore likely that, as the main channel stage fell, flood waters stored  
473 on the floodplain were transferred back to the main channel due to the increased  
474 hydraulic gradient between the floodplain and channel.

475

476 During the rising limb, the suspended sediment flux recorded upstream of the  
477 bifurcation was  $2,150 \pm 430 \text{ kg s}^{-1}$ . For suspended sediment estimates, we assume an  
478 error of 20% which equates to one standard deviation of the flux estimates derived  
479 from the four individual transect passes at XS001 across all three survey seasons. At  
480 the downstream limit of the reach, the load recorded was  $2,000 \pm 400 \text{ kg s}^{-1}$ , thus a  
481 loss of  $150 \pm 830 \text{ kg s}^{-1}$  (12%) occurred across the unit at this flow stage. As can be  
482 seen in Figure 7 a and b, approximately  $1,500 \pm 1,166 \text{ kg s}^{-1}$  of additional sediment  
483 was remobilised as suspended load between XS001 and XS002, around the bar head  
484 on C<sub>1</sub>. This additional suspended load persisted until XS004A, after which a decrease  
485 of  $1,420 \pm 1,004 \text{ kg s}^{-1}$  was recorded (Figure 7 a and b). However, taken over the  
486 course of the entire diffluence-confluence unit the sediment flux appears to be in  
487 balance, with deposition at the island head approximately balancing erosion at the tail  
488 of the island, and no significant net loss or gain of suspended sediment between the  
489 upstream bifurcation and downstream confluence.

490

491 **[INSERT FIGURE 7 HERE]**

492

493 During high flows, a sediment flux of  $6,300 \pm 1,260 \text{ kg s}^{-1}$  was measured entering the  
494 diffluence-confluence unit whereas  $3,700 \pm 740 \text{ kg s}^{-1}$  exited the reach at XS007. This  
495 represents a transmission loss of  $2,600 \pm 2,000 \text{ kg s}^{-1}$  (41%) across the unit. As can  
496 be seen in Figure 7 c and d, this loss was systematic down both C<sub>1</sub> and C<sub>2</sub> (specifically,  
497 the downstream portion of C<sub>2</sub>) although between each individual link in the unit, no  
498 loss exceeds its error; it is only the summative loss between XS001 and XS007 that  
499 shows a significant loss of suspended sediment. Although no significant losses exist

500 throughout the unit, potential hotspots of sediment deposition can be postulated, most  
501 notably between XS002 and XS003A on C<sub>1</sub> where  $\sim 1,400 \pm 1,880 \text{ kg s}^{-1}$  was lost. This  
502 location is the site of a smaller bifurcation within C<sub>1</sub> (see Figure 1A). No measurements  
503 were possible within the subsidiary channels at this flow stage (due to the shallow  
504 water preventing access by the survey vessels), so we are unable to directly assess  
505 the distribution of suspended sediment at this specific bifurcation. However, this region  
506 is characterised by well-developed bar-head deposits (see satellite images in Figures  
507 1A, 6 and 7), so it is possible that sediment was being deposited on the bar head at  
508 this location during this period. Federici and Paola (2003) and Bolla Pittaluga et al.  
509 (2003) found that stable bars form at bifurcations with high Shields numbers. Data  
510 from XS002 and XS003A suggest that between these two transects there is a large  
511 increase in the Shields number ( $\theta$ ), here defined as

$$512 \quad \theta = \frac{\tau}{(\rho_s - \rho)gD_{50}} \quad (6)$$

513 where  $\tau$  is the bed shear stress ( $\text{N m}^{-2}$ ),  $\rho_s$  is the density of the sediment ( $\text{kg m}^{-3}$ ),  $\rho$  is  
514 the water density ( $\text{kg m}^{-3}$ ),  $g$  is acceleration due to gravity ( $\text{m s}^{-2}$ ;  $9.81 \text{ m s}^{-2}$ ) and  $D_{50}$   
515 is the median bed grain size (m; 0.002 m), with  $\theta$  increasing from 0.09 to 2.1. We note  
516 that our estimates of the Shields parameter have an error of  $\sim 13\%$  resulting from the  
517 use of aDcp velocity data to calculate  $\tau$  and in the particle size analysis ( $\sim 3\%$ ;  
518 manufacturer specification for Saturn Digisizer).

519

520 It is possible that the development of a bar in the bifurcation just upstream of XS003A  
521 may account for the loss in suspended sediment through this section. An alternative  
522 possibility is that the suspended sediment may be being preferentially partitioned down  
523 the smaller bifurcate channel. However, this is unlikely as when the smaller bifurcate

524 re-joins the main channel (just below XS004A; see Figure 1A), there is no  
525 commensurate increase in suspended sediment load at XS005 (Figure 7 c and d).  
526 Similarly, as little sediment was lost between XS003A and XS004A (Figure 7 c and d),  
527 it is more likely that sediment was being deposited around the bifurcation between  
528 XS002 and XS003A, perhaps in bar head deposits.

529

530 Analysis of the mean annual flow hydrograph at Kampong Cham (Figure 1B) reveals  
531 that flows in excess of  $27,000 \text{ m}^3 \text{ s}^{-1}$  occur for approximately 78 days a year. Assuming  
532 that the sediment loss of  $2,600 \pm 2,600 \text{ kg s}^{-1}$  is maintained over those 78 days, the  
533 average volume of sand lost at this location would amount to at least  $63,882 \text{ m}^3$  (based  
534 on a density of sand of  $1,920 \text{ kg m}^{-3}$ ). The area of the study reach (the difffluence-  
535 confluence unit) as measured from Landsat imagery is  $\sim 33 \text{ km}^2$  (Figure 8b). The  
536 volumetric sand loss therefore equates to a  $0.002 \text{ m}$  deposit of sediment uniformly  
537 spread across the confluence-difffluence unit during an 'average' flood season.  
538 However, as we show in Figure 7, the deposition is not uniform and therefore depths  
539 of deposits are likely to be higher in some locations. For example, assuming deposition  
540 only occurs in the area of bar head deposits between XS002 and XS003A (shown to  
541 be a sink in Figure 7), this area of  $1.9 \text{ km}^2$  would experience a deposit depth of  $3 \text{ cm}$   
542 if all sediment was deposited here across a flood season.

543

544 A further potential sink of suspended sediment at high flows appears at the  
545 downstream end of the reach, with  $400 \pm 1,520 \text{ kg s}^{-1}$  being lost between XS005 and  
546 XS006. The aerial images reveal no obvious bar deposits in this vicinity (Figures 1A).  
547 To assess whether material was being stored in this potential sink zone, selected  
548 georeferenced aerial photos from 1959 and Landsat images over the period 1973 to

549 2013 (selected on the basis of being cloud free and all being taken within the same  
550 calendar month to ensure similar flow stage) were analysed and the areal extent of  
551 the island complex was delineated (Figure 8). This analysis shows that the island  
552 complex has been prograding at its downstream extent at a rate of approximately 0.05  
553 km<sup>2</sup> a<sup>-1</sup> since 1973 ( $R^2 = 0.4$ ,  $p = 0.5$ ; Figure 8). This prograding area corresponds to  
554 the region between cross-section XS006 and XS007 and thus precisely to the zone  
555 where, at high flows, a sink of suspended sediment was inferred. Therefore, it is likely  
556 that this sink zone is actively depositing when flow stage is greater than the mean  
557 annual flow ( $\sim 14,500 \text{ m}^3 \text{ s}^{-1}$ ), causing the downstream progradation of the island  
558 complex.

559

560 **[INSERT FIGURE 8 HERE]**

561

562 During the falling limb of the hydrograph,  $1,000 \pm 200 \text{ kg s}^{-1}$  of sediment was estimated  
563 to be entering the unit, with  $830 \pm 166 \text{ kg s}^{-1}$  exiting at its southernmost extent. This  
564 represents a net loss of 17% of the incoming sediment load ( $170 \pm 366 \text{ kg s}^{-1}$ ). At this  
565 flow stage, both C<sub>1</sub> and C<sub>2</sub> display relatively stable links in its downstream extent, with  
566 the largest gain of  $13 \pm 8.4 \text{ kg s}^{-1}$  occurring between XS003B and XS004B. This gain  
567 is likely associated with a remobilisation of sediment sequestered into this smaller  
568 subsidiary channel during the higher flow flood period.

## 569 **Discussion**

570 The results shown in Figure 7 suggest that different regions of the diffluence-  
571 confluence unit become active at different flow stages and that individual links within



572 the unit may display different behaviour (net erosion and net deposition) at different  
573 flow stages. These differences are likely to be in part controlled by the partitioning of  
574 the flow and sediment at the bifurcation at the head of the diffluence-confluence unit,  
575 as variations here will impact morphodynamics downstream. To assess how this  
576 partitioning varies with flow stage we define the discharge asymmetry ratio of the  
577 bifurcation ( $Q_{r^*}$ ) following Kleinhans et al. (2013) such that:

$$578 \quad Q_{r^*} = (Q_1 - Q_2)/Q_0 \quad (8)$$

579 where  $Q_0$  is the discharge in the main channel upstream of the bifurcation. As values  
580 of  $Q_{r^*}$  tend towards unity, the distribution of water at the bifurcation becomes more  
581 uneven, with more flow discharge being routed down the primary channel ( $C_1$ ) of the  
582 bifurcation. As values approach zero, flow discharge is evenly split between the  
583 channels.

584

585 Our data show that the discharge asymmetry ratio declined from a value of  $Q_{r^*} = 0.54$   
586 during the high flow of the monsoon flood-pulse (September 2013,  $Q = 27,000 \text{ m}^3 \text{ s}^{-1}$ )  
587 to  $Q_{r^*} = 0.44$  on the falling limb of the hydrograph (October 2013,  $Q = 13,500 \text{ m}^3 \text{ s}^{-1}$ )  
588 and subsequently rose to a value of 0.59 on the following rising limb of the  
589 hydrograph (July 2014;  $Q = 19,500 \text{ m}^3 \text{ s}^{-1}$ ). This suggests that the  $Q_{r^*}$  fluctuates with  
590 discharge and between flood events, with the low flow period between October 2013  
591 and July 2014 representing a time when the bifurcation becomes more unstable ( $Q_{r^*}$   
592 values increase towards unity). It also suggests that over the course of the flood  
593 (September 2013 and October 2013) the flow partitioning within the bifurcation  
594 becomes more symmetrical (i.e.,  $Q_{r^*}$  values tend closer towards zero). Zolezzi et al.  
595 (2006) and Szupiany et al. (2012) also report that bifurcations tend to become more

596 symmetrical as discharge increases. Our data show that bifurcations become more  
597 symmetrical across a single flood wave with increasing discharge, but that this  
598 symmetry does not necessarily track variations in flow discharge in a straightforward  
599 manner. For example, discharges were higher in July 2014 ( $19,500 \text{ m}^3 \text{ s}^{-1}$ ) than in  
600 October 2013 ( $13,500 \text{ m}^3 \text{ s}^{-1}$ ), but asymmetry was greater for the higher magnitude of  
601 the two flows ( $Q_r^* = 0.59$  compared to  $0.44$ ). Furthermore, comparison to the data in  
602 Figure 7 suggests that a more equal split of discharge down each bifurcate channel  
603 (October 2013;  $Q_r^* = 0.44$ ) results in less variation in the suspended sediment budget  
604 through the diffidence-confluence unit (Figure 7) that when discharge asymmetry is  
605 greater. As discharge is partitioned more unequally, localised zones of erosion and  
606 deposition begin to become active throughout the diffidence-confluence unit (Figure  
607 7). Therefore, the initial distribution of discharge at the bifurcation likely plays a key  
608 role in determining the behaviour of the unit downstream.

609

610 The distribution of discharge between the two channels of a bifurcation has been  
611 shown to be controlled by cross-stream water surface slopes (Zolezzi et al., 2006;  
612 Szupiany et al., 2012), bed slope (Kleinhans et al., 2008; Hardy et al., 2011) and  
613 upstream curvature (Kleinhans et al., 2008; Thomas et al., 2012; Marra et al., 2013)  
614 amongst many other factors. The results presented above allow us to assess the role  
615 of these factors on a large river bifurcation. As discussed above variations in cross-  
616 stream water surface slope are present between the surveys (Figure 4A). We find that  
617 the lowest water surface slopes ( $3 \times 10^{-5} \text{ m m}^{-1}$ ; October 2013;  $Q = 13,500 \text{ m}^3 \text{ s}^{-1}$ )  
618 correspond to the most equal distribution of discharge at the bifurcation ( $Q_r^* = 0.44$ ).  
619 However, although water surface slopes increase with discharge it does not follow that  
620 an increase in water surface slope leads to more unequal partitioning of discharge at

621 the bifurcation. During the highest flows observed (September 2013;  $Q = 27,000 \text{ m}^3 \text{ s}^{-1}$ )  
622  $^1$ ), water surface slopes were  $8 \times 10^{-5} \text{ m m}^{-1}$  whilst in July 2014, when  $Q = 19,500 \text{ m}^3$   
623  $\text{s}^{-1}$ , water surface slopes were  $4 \times 10^{-5} \text{ m m}^{-1}$ . However,  $Q_{r^*}$  during September 2013  
624 equated to 0.54 whilst in July 2014  $Q_{r^*}$  equated to 0.59. Thus the highest water surface  
625 slopes do not correspond to the greatest asymmetry in flow. It is therefore likely the  
626 bed morphological changes shown in Figure 5 that occurred between October 2013  
627 and July 2014 result in a topographic steering of the flow which dominates over the  
628 cross-stream water slope with respect to the distribution of the water and sediment  
629 between the two bifurcate channels.

630

631 The morphological changes may then impact on future distributions of water and  
632 sediment through the bifurcating channels, and in doing so, potentially shift the  
633 bifurcation towards a different equilibrium state. In both fine-grained and coarse-  
634 grained systems, the equilibrium configuration of bifurcations has been estimated  
635 using numerical modelling techniques (Bolla Pittaluga et al. 2003, Edmonds and  
636 Slingerland, 2008; Bolla Pittaluga et al. 2015), though available field data to test these  
637 theories has, as discussed previously, to date been lacking. The availability of our field  
638 data therefore provides an opportunity to compare the stability diagrams produced  
639 from these theoretical studies with real world data, provided the dimensional and non-  
640 dimensional parameter space observed in the real world data conforms to that used  
641 in the numerical studies. For example, the stability curve of Bolla Pittaluga et al. (2003)  
642 was derived with a half width-depth ratio,  $\beta$ , of 8 and a dimensionless Chezy coefficient,  
643  $C_a$ , of 12.5, where the non-dimensional Chezy coefficient is defined following Bolla  
644 Pittaluga et al. (2015) such that:

645 
$$C_a = 6 + 2.5 \log\left(\frac{d}{2.5D_{50}}\right) \quad (9)$$

646 where  $d$  is the channel depth (m).

647

648 For the cross-section at the head of the bifurcation on the Mekong, values of  $C_a$  vary  
649 from 15 (September 2013) to 17 (October 2013 and July 2014). The respective values  
650 of  $\beta$  are approximately 25 across all three survey periods. These values mean it is not  
651 valid to compare the data for the Mekong to the stability curves proposed by Bolla  
652 Pittaluga et al. (2003) or Edmonds and Slingerland (2008), both of which have similar  
653 parameter values ( $C_a = 12.5$ ,  $\beta = 8$ ). However, it is possible to compare our observed  
654 data to the stability criteria proposed in Bolla Pittaluga et al. (2015), whose stability  
655 phase space contains multiple curves for varying values of  $\beta$ . Indeed, one such curve  
656 in their phase space equates to  $\beta = 25$ . Values of  $C_a$  for these curves equal 13, and  
657 although this is not exactly identical to the values observed for the Mekong (15 to 17),  
658 it is a closer fit to the observed data than other available stability diagrams.  
659 Furthermore, Bolla Pittaluga et al. (2015) suggest that their stability relationships are  
660 only slightly sensitive to variations in  $C_a$ . Therefore, it is reasonable to compare our  
661 observed data to this proposed stability curve. Furthermore, we acknowledge that  
662 these stability diagrams are also based on the assumption of downstream equal width  
663 channels, whereas on the Mekong we observe downstream channels of unequal width  
664 ( $C_1 = 1400$  m wide,  $C_2 = 700$  m wide). Miori et al. (2006) explore the effect of removing  
665 the assumption of equal downstream channel widths on the stability phase space,  
666 demonstrating that the qualitative behaviour tending towards equilibrium is not  
667 affected by varied width channels, though the time taken to reach that stable state is  
668 affected. As we are not looking at a long temporal sequence of bifurcation stability,

669 rather snapshots across a single flood wave, it is again justifiable to compare the  
670 Mekong to the stability phase space of Bolla Pittaluga et al. (2015).

671

672 The behaviour of the Mekong bifurcation when plotted against the Bolla Pittaluga et al.  
673 (2015) stability diagrams (Figure 9) depends upon the sediment transport regime  
674 (bedload or suspended load) dominant at the bifurcation. Bolla Pittaluga et al. (2015)  
675 define stability phase spaces for both bedload and suspended load dominant systems,  
676 using the Van Rijn (1984) sediment transport equation (Figure 9a) for suspended load  
677 and a combination of the Meyer-Peter Müller (MPY; 1948) regime for gravel beds and  
678 the Engelund and Hansen (EH; 1967) sand-bed relationship (Figure 9b) for bedload  
679 transport regimes. Assuming for the moment a suspended sediment dominant  
680 scenario (Figure 9a), our field data indicate that at the lowest discharge (October 2013;  
681  $Q = 13,500 \text{ m}^3 \text{ s}^{-1}$ ) the bifurcation is in fact in an equilibrium configuration (as defined  
682 by Bolla Pittaluga et al., 2015). At the highest observed discharge (September 2013;  
683  $Q = 27,000 \text{ m}^3 \text{ s}^{-1}$ ) the bifurcation is again within the stable phase space proposed by  
684 Bolla Pittaluga et al. (2015) due to the considerably lower Shields number for the value  
685 of  $Q_{r^*}$  observed. This reflects the coarsening of the bed material observed at this flow,  
686 increasing from medium sand ( $\sim 0.4 \text{ mm}$ ) on the rising and falling limbs, to coarse sand  
687 ( $2 \text{ mm}$ ) during high flows, and therefore likely a transition away from suspended  
688 sediment dominant conditions. On the rising limb (July 2014;  $Q = 19,500 \text{ m}^3 \text{ s}^{-1}$ ), the  
689 bifurcation transitions into the unstable phase space due to an increase in Shields  
690 number which is not matched by an increase in discharge asymmetry. This behaviour  
691 is corroborated by our field observations of suspended sediment load through the  
692 diffluence-confluence unit which shows significant net erosion and deposition of  
693 suspended sediment only during the rising limb of the hydrograph (Figure 7b).

694

695 Conversely, if we assume the bifurcation operates under a bedload dominated  
696 scenario (Figure 9b) the bifurcation is predicted to behave similarly, although it never  
697 fully transitions into an unstable phase space. During high flows (September 2013;  $Q$   
698 = 27,000  $\text{m}^3\text{s}^{-1}$ ) the bifurcation is predicted to be in a stable state, transitioning first to  
699 the unstable phase space at low flow (October 2013;  $Q = 13,500 \text{ m}^3 \text{ s}^{-1}$ ), before  
700 transitioning back to the boundary of the stable-unstable phase space during the rising  
701 limb (July 2014;  $Q = 19,500 \text{ m}^3 \text{ s}^{-1}$ ). This pattern conforms to that reported by Zolezzi  
702 et al. (2006) and Szupiany et al. (2012) who propose more stable bifurcations at higher  
703 discharges. It is noteworthy that the highest flow discharge we observed (27,000  $\text{m}^3$   
704  $\text{s}^{-1}$ ) is still just ~50% of the mean annual peak flood value (52,500  $\text{m}^3 \text{ s}^{-1}$ ).

705

706 **[INSERT FIGURE 9 HERE]**

707

708 Nevertheless, given the average annual discharge at Kampong Cham is 14,500  $\text{m}^3 \text{ s}^{-1}$   
709 <sup>1</sup>, it is likely that the bifurcation that is the specific focus of this study spends the  
710 majority of time in a near-stable configuration, regardless of the dominant transport  
711 regime. This may suggest that large river bifurcations may form profiles at near-  
712 equilibrium configurations at mean-to-low flows, which are the most common  
713 throughout the hydrograph. Edmonds and Slingerland (2008) note that stable fine-  
714 grained bifurcations are resistant to perturbations, returning to an equilibrium  
715 configuration over time. The mode of dominant sediment transport (bedload versus  
716 suspended load) has long been identified as a control on river morphology (Schumm,

717 1985; Church, 2006) and recent modelling work has highlighted the key role  
718 suspension of bed material plays in defining large river channel planforms (Nicholas,  
719 2013). Our observations suggest that under differing dominant regimes, the bifurcation  
720 will behave differently, therefore understanding the dominant mode of sediment  
721 transport in large rivers is key to understanding and predicting large river bifurcation  
722 stability and larger planform change, over longer time frames.

723

## 724 **Conclusion**

725 This paper reports observations from a bifurcation and associated diffluence-  
726 confluence unit on a reach of one of the world's largest rivers, the Mekong in Cambodia.  
727 Through the use of high-resolution aDcp flow monitoring and MBES bathymetric  
728 surveys across the flood wave, we reveal that bifurcation discharge asymmetry falls  
729 from 0.54 at high flows ( $27,000 \text{ m}^3 \text{ s}^{-1}$ ) in September 2013 to 0.44 during the falling  
730 limb of the flood in October 2013 ( $13,500 \text{ m}^3 \text{ s}^{-1}$ ), but increasing back up to 0.59 in July  
731 2014 ( $19,500 \text{ m}^3 \text{ s}^{-1}$ ). Our results reveal that flow discharge is not the sole control on  
732 bifurcation asymmetry; rather, fluctuations in bifurcation asymmetry appear to be the  
733 result of multiple processes operating in tandem, including varying flow discharge, bed  
734 morphological change and the influence of cross-stream water surface slopes. The  
735 influence of flow discharge is more keenly expressed throughout the diffluence-  
736 confluence unit downstream of the bifurcation, where the island complex acts as a sink  
737 of suspended sediment during high flows (with a net loss of  $2,600 \pm 2,000 \text{ kg s}^{-1}$ ), but  
738 appears to be in quasi-equilibrium distribution during the rising and falling stages. We  
739 show that large river bifurcation stability is dependent on the dominant sediment  
740 transport regime (bedload versus suspended load) and that transitions to instability

741 occur at different points on the hydrograph dependent upon the changing relative  
742 dominance of the mechanism of transport. A deeper appreciation of the dominant  
743 transport mechanisms of the world's largest rivers is, therefore, necessary in order to  
744 better predict and understand their planform change and channel behaviour dynamics.

#### 745 **Acknowledgments**

746 This research was supported by awards NE/JO21970/1, NE/JO21571/1 and  
747 NE/JO21881/1 (to Southampton, Exeter and Hull, respectively) from the UK Natural  
748 Environment Research Council (NERC). We gratefully acknowledge the assistance of  
749 the Mekong River Commission, the Department of Hydrology and Water Resources  
750 (DHRW), Cambodia and Mr. Ben Savuth, Cpt. Thy and Cpt. Horn, and the DHRW  
751 research vessel crews for their assistance and company in the field.

#### 752 **References**

753 Aalto, R., Lauer, JW & Dietrich, WE. (2008) Spatial and Temporal Dynamics of  
754 Sediment Accumulation and Exchange along Strickland River Floodplains (Papua  
755 New Guinea) over Decadal-to-Centennial Timescales, *Journal of Geophysical*  
756 *Research: Earth Surface* 113: 1–22, doi:10.1029/2006JF000627.

757 Aalto, R, Maurice-bourgoin, L & Dunne, T. (2003) Episodic Sediment Accumulation on  
758 Amazonian Flood Plains Influenced by El Nino/Southern Oscillation, *Nature* 425  
759 (October): 493–497, doi:10.1038/nature02002.

760 Adamson, PT, Rutherford, ID, Peel, MC & Conlan, IA. (2009) The Hydrology of the  
761 Mekong River, *In: Campbell, IC (eds). The Mekong: Biophysical environment of an*  
762 *international river basin*, Amsterdam: Elsevier, p.432



763 Bolla Pittaluga, M, Repetto, R & Tubino, M. (2003) Channel Bifurcation in Braided  
764 Rivers: Equilibrium Configurations and Stability, *Water Resources Research* 39 (3):  
765 1–13, doi:10.1029/2001WR001112.

766 Bolla Pittaluga, M, Coco, G & Kleinhans, MG (2015), A unified framework for stability  
767 of channel bifurcations in gravel and sand fluvial systems, *Geophysical Research*  
768 *Letters*, 42, 7521–7536, doi:10.1002/2015GL065175

769 Bridge, JS. (1993) The Interaction between Channel Geometry, Water Flow, Sediment  
770 Transport and Deposition in Braided Rivers, *Geological Society, London, Special*  
771 *Publications* 75 (75): 13–71

772 Carling, PA. (2009) The Geology of the Lower Mekong River, *In: The Mekong:*  
773 *Biophysical environment of an international river basin*, pp.13–28

774 Church, M. (2006) Bed material transport and the morphology of alluvial river  
775 channels, *Annual Reviews of Earth and Planetary Sciences*, v. 34, p. 325 - 354. doi:  
776 10.1146/annurev.earth.33.092203.122721.

777 Constantine, JA, Dunne, T, Ahmed, J, Legleiter, C & Lazarus, ED. (2014) Sediment  
778 Supply as a Driver of River Evolution in the Amazon Basin, *Nature Geoscience* 7: 1–  
779 23, doi: 10.1038/NGEO2282.

780 Darby, SE, Rinaldi, M & Dapporto, S (2007) Coupled simulations of fluvial erosion and  
781 mass wasting for cohesive river banks, *Journal of Geophysical Research*, 112, F03022,  
782 doi:10.1029/2006JF000722.

783 Darby, SE, Trieu, HQ, Carling, PA, Sarkkula, J, Koponen, J, Kummu, M, Conlan, I &  
784 Leyland, J. (2010) A physically based model to predict hydraulic erosion of fine-

785 grained riverbanks: The role of form roughness in limiting erosion, *Journal of*  
786 *Geophysical Research*, 115, F04003, doi: 10.1029/2010JF001708.

787 Darby, SE, Leyland, J, Kummu, M, Räsänen, TA & Lauri, H. (2013) Decoding the  
788 Drivers of Bank Erosion on the Mekong River: The Roles of the Asian Monsoon,  
789 Tropical Storms, and Snowmelt, *Water Resources Research* 49,  
790 doi:10.1002/wrcr.20205

791 Darby, SE, Hackney, CR, Leyland, J, Kummu, M, Lauri, H, Parsons, DR, Best, JL,  
792 Nicholas, AP, Aalto, R. (2016) Fluvial sediment supply to a mega-delta reduced by  
793 shifting tropical-cyclone activity, *Nature*, 539, 276 - 279, doi: 10.1038/nature19809.

794 Eaton, BC, Millar, RG & Davidson, S. (2010) Channel Patterns: Braided, Anabranching,  
795 and Single-Thread, *Geomorphology* 120 (3-4): 353–364,  
796 doi:10.1016/j.geomorph.2010.04.010

797 Edmonds, DA & Slingerland, RL. (2008) Stability of Delta Distributary Networks and  
798 Their Bifurcations, *Water Resources Research* 44 (9). doi: 10.1029/2008WR006992

799 Engel, FL & Rhoads, BL. (2016) Three-dimensional flow structure and patterns of bed  
800 shear stress in an evolving compound meander bend, *Earth Surface Processes and*  
801 *Landforms*, doi: 10.1002/esp.3895

802 Engelund, F and Hansen, E. (1967) *A monograph on sediment transport in alluvial*  
803 *streams*, Tech. Univ. of Denmark, Technisk Forlag, Copenhagen, Denmark.

804 Gupta, A & Liew, SC. (2007) The Mekong from Satellite Imagery: A Quick Look at a  
805 Large River, *Geomorphology* 85 (3-4): 259–274, doi:10.1016/j.geomorph.2006.03.036

806 Hackney, C & Carling, PA. (2011) The Occurrence of Obtuse Junction Angles and  
807 Changes in Channel Width below Tributaries along the Mekong River, South-East Asia,  
808 *Earth Surface Processes and Landforms* 36 (12): 1563–1576, doi:10.1002/esp.2165

809 Hardy, RJ, Lane, SN & Yu, D. (2011) Flow Structures at an Idealized Bifurcation: A  
810 Numerical Experiment, *Earth Surface Processes and Landforms* 36 (October): 2083–  
811 2096, doi:10.1002/esp.2235.

812 Kleinhans, MG, Jagers, HRA, Mosselman, E & Sloff, CJ. (2008) Bifurcation Dynamics  
813 and Avulsion Duration in Meandering Rivers by One-Dimensional and Three-  
814 Dimensional Models, *Water Resources Research* 44 (8): W08454,  
815 doi:10.1029/2007WR005912.

816 Kleinhans, MG, Cohen, KM, Hoekstra, J & Ijmker, KM. (2012) Evolution of a bifurcation  
817 in a meandering river with adjustable channel widths, Rhine delta apex, The  
818 Netherlands, *Earth Surface Processes and Landforms*, 36, 15, 2011 - 2027, doi:  
819 10.1002/esp.2222.

820 Kleinhans, MG, Ferguson, RI, Lane, SN & Hardy, RJ. (2013) Splitting Rivers at Their  
821 Seams: Bifurcations and Avulsion, *Earth Surface Processes and Landforms* 38 (June  
822 2012): 47–61, doi:10.1002/esp.3268.

823 Kostaschuk, R., Best, J, Villard, P, Peakall, J & Franklin, M. (2005) Measuring Flow  
824 Velocity and Sediment Transport with an Acoustic Doppler Current Profiler,  
825 *Geomorphology* 68 (1-2): 25–37, doi:10.1016/j.geomorph.2004.07.012

826 Kumm, M, Lu, XX, Rasphone, A, Sarkkula, J & Koponen, J. (2008) Riverbank  
827 Changes along the Mekong River: Remote Sensing Detection in the Vientiane–Nong

828 Khai Area, *Quaternary International* 186 (1): 100–112,  
829 doi:10.1016/j.quaint.2007.10.015

830 Latrubesse, EM. (2008) Patterns of Anabranching Channels: The Ultimate End-  
831 Member Adjustment of Mega Rivers, *Geomorphology* 101 (1-2): 130–145,  
832 doi:10.1016/j.geomorph.2008.05.035

833 Lane, S.N., Bradbrook, K., Richards, K.R., Biron, P.M. & Roy, A.G. (2000) Secondary  
834 circulation cells in river channel confluences: measurement artefacts or coherent flow  
835 structures? *Hydrological Processes*, 14, 2047 - 2071.

836 Leopold, LB & Wolman, MG. (1957) *River Channel Patterns: Braided, Meandering and*  
837 *Straight*, Washington D.C

838 Marra, WA, Parsons, DR, Kleinhans, MG, Keevil, GM & Thomas, RE. (2014) Near-  
839 Bed and Surface Flow Division Patterns in Experimental River Bifurcations, *Water*  
840 *Resources Research* 50: 1506–1530, doi:10.1002/2013WR014215.

841 McLelland, SJ, Ashworth, PJ, Best, JL, Roden, J & Klaassen, GJ. (1990) Flow  
842 Structure and Transport of Sand-Grade Suspended Sediment around an Evolving  
843 Braid Bar, Jamuna River, Bangladesh, *Special Publication of the International*  
844 *Association of Sedimentologists* 28: 43–57

845 Meyer-Peter, E and Müller, R. (1948) Formulas for bedload transport, Proc. Second  
846 Congress: Stockholm. *International Association of Hydraulic Structures Research*, 30:  
847 3203 - 3212.

848 Milliman, JD & Farnsworth, KL. (2011) *River discharge to the global ocean: A global*  
849 *synthesis*, Cambridge University Press, Cambridge, UK.

850 Milliman, JD & Syvitski, JPM. (1992) Geomorphic/Tectonic Control of Sediment  
851 Discharge to the Ocean: The Importance O F Small Mountainous Rivers<sup>1</sup>, *Journal of*  
852 *Geology* 100: 525 – 544

853 Miori, S., Repetto, R., Tubino, M. (2006) A one-dimensional model of bifurcations in  
854 gravel bed channels with erodible banks, *Water Resources Research*, 42, 11,  
855 doi:10.1029/2006WR004863.

856 MRC. (2009) *The Flow of the Mekong*, Mekong River Commission Secretariate,  
857 Vientiane.

858 Mueller, DS & Wagner, CR. (2009) *Measuring discharge with acoustic Doppler current*  
859 *profilers from a moving boat: U.S. Geological Survey Techniques and Methods 3A-22*,  
860 72 p.

861 Nicholas, A.P. (2013) Morphodynamic diversity of the world's largest rivers, *Geology*,  
862 41, 4, 475 -478. doi: 10.1130/G34016.1

863 Parker, G. (1991) Selective sorting and abrasion of river gravel. II: Applications.  
864 *Journal of Hydraulic Engineering, ASCE*, 117(2):150 - 171. doi:10.1061/(ASCE)0733-  
865 9429(1991)117:2(150).

866 Parsons, DR, Best, JL, Lane, SN, Orfeo, O, Hardy, RJ & Kostaschuk, R. (2007) Form  
867 Roughness and the Absence of Secondary Flow in a Large Confluence–difffluence,  
868 Rio Paraná, Argentina, *Earth Surface Processes and Landforms* 32 (1): 155–162,  
869 doi:10.1002/esp.1457

870 Parsons, DR, Jackson, PR, Czuba, JA, Engel, FL, Rhoads, BL, Oberg, KA, Best, JL,  
871 Mueller, DS, Johnson, KK & Riley, JD. (2013) Velocity Mapping Toolbox (VMT): A

872 Processing and Visualization Suite for Moving-Vessel ADCP Measurements, *Earth*  
873 *Surface Processes and Landforms* 38 (11): 1244 – 1260, doi: 10.1002/esp.3367.

874 Richardson, WR & Thorne, CR. (2001) Multiple Thread Flow and Channel Bifurcation  
875 in a Braided River: Brahmaputra-Jamuna River, Bangladesh, *Geomorphology* 38:  
876 185–196

877 Schumm, SA. (1985) Patterns of Alluvial Rivers, *Annual Review of Earth and Planetary*  
878 *Sciences* 13: 5–27

879 Shugar, DH, Kostaschuk, R, Best, JL, Parsons, DR, Lane, SN, Orfeo, O, Hardy, RJ.  
880 (2010) On the Relationship between Flow and Suspended Sediment Transport over  
881 the Crest of a Sand Dune, Rio Parana, Argentina, *Sedimentology* 57 (1): 252–272,  
882 doi:10.1111/j.1365-3091.2009.01110.x

883 Szupiany, RN, Amsler, ML, Best, JL & Parsons, DR. (2007) Comparison of Fixed- and  
884 Moving-Vessel Flow Measurements with an aDp in a Large River, *Journal of*  
885 *Hydrologic Engineering* 133: 1299–1309

886 Szupiany, RN, Amsler, ML, Hernandez, J, Parsons, DR, Best, JL, Fornari, E, & Trento,  
887 A. (2012) Flow Fields, Bed Shear Stresses, and Suspended Bed Sediment Dynamics  
888 in Bifurcations of a Large River, *Water Resources Research* 48: 1–20.  
889 Doi:10.1029/2011WR011677.

890 Szupiany, RN, Amsler, ML, Parsons, DR & Best, JL. (2009) Morphology, Flow  
891 Structure, and Suspended Bed Sediment Transport at Two Large Braid-Bar  
892 Confluences, *Water Resources Research* 45, W05415, doi: 10.1029/2008WR007428.

893 Thomas, RE, Parsons, DR, Sandbach, SD, Keevil, GM, Marra, WA, Hardy, RJ, Best,  
894 JL, Lane, SN & Ross, JA. (2011) An Experimental Study of Discharge Partitioning and  
895 Flow Structure at Symmetrical Bifurcations, *Earth Surface Processes and Landforms*  
896 36: 2069–2082. Doi:10.1002/esp.2231.

897 van Rijn, LC. (1984) Sediment transport part II: Suspended load transport. *Journal of*  
898 *Hydraulic Engineering*, 110(11), 1431 - 1456.

899 Whiting, PJ & Dietrich, WE. (1990) Boundary shear stress and roughness over mobile  
900 alluvial beds. *Journal of Hydraulic Engineering, ASCE*, 116(12):1495 – 1511.  
901 Doi:10.1061/(ASCE)0733-9429(1990)116:12(1495).

902 Zolezzi, G, Bertoldi, W, Turbino, M. (2006) Morphological analysis and prediction of  
903 river bifurcations. In *Braided Rivers: Processes, Deposits, Ecology and Management*,  
904 Sambrook Smith GH, Best JL, Bristow CS & Petts GE (eds). International Association  
905 of Sediment Special Publication 36: Malden, MA; 233 – 256.

906

907

908

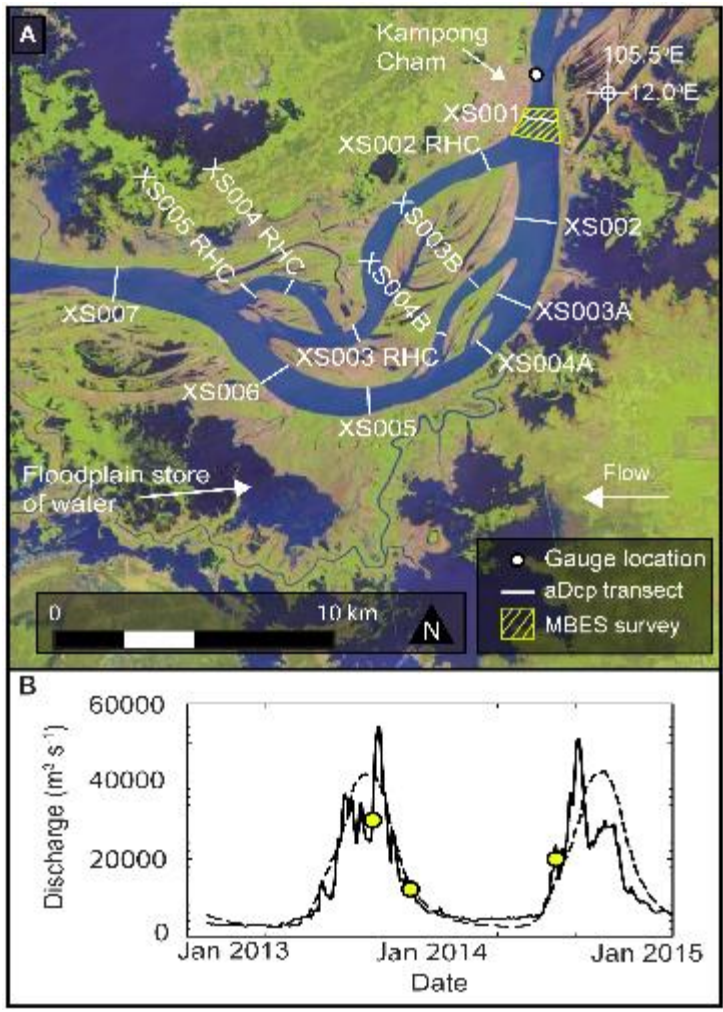
909

910

911

912

913

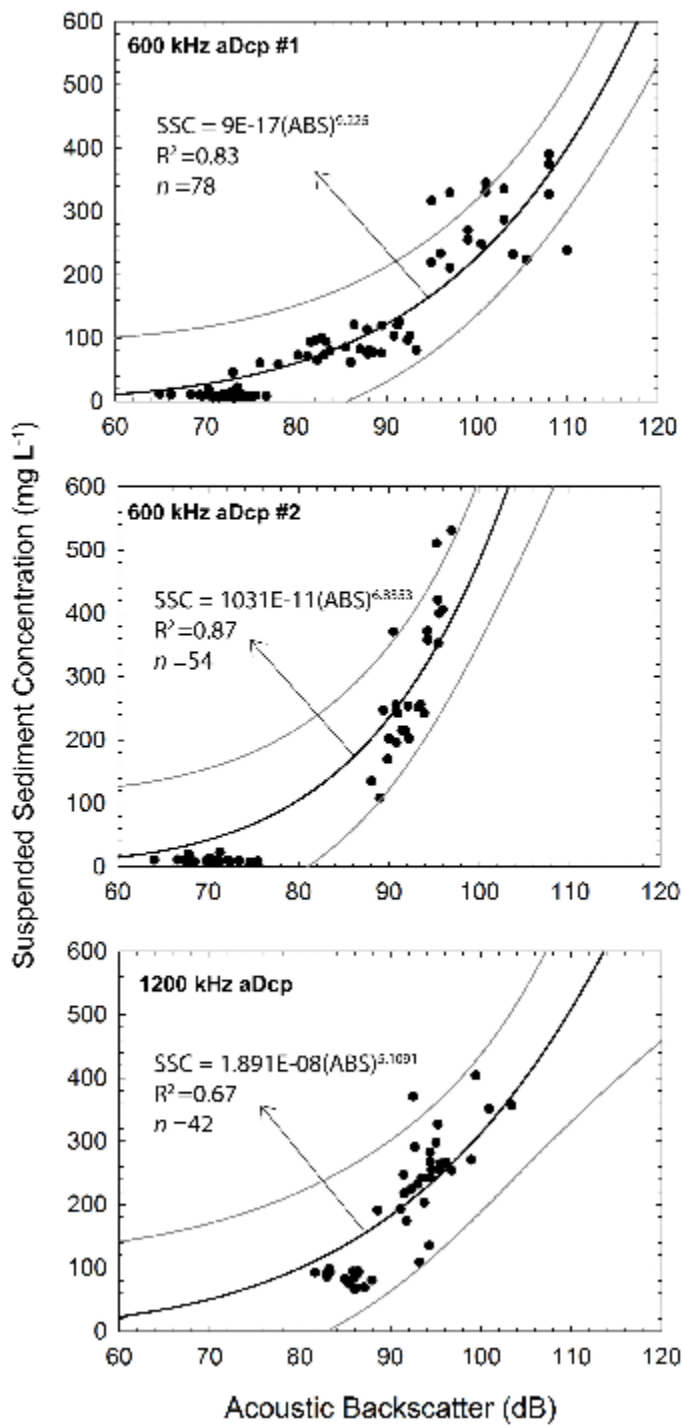


914

915

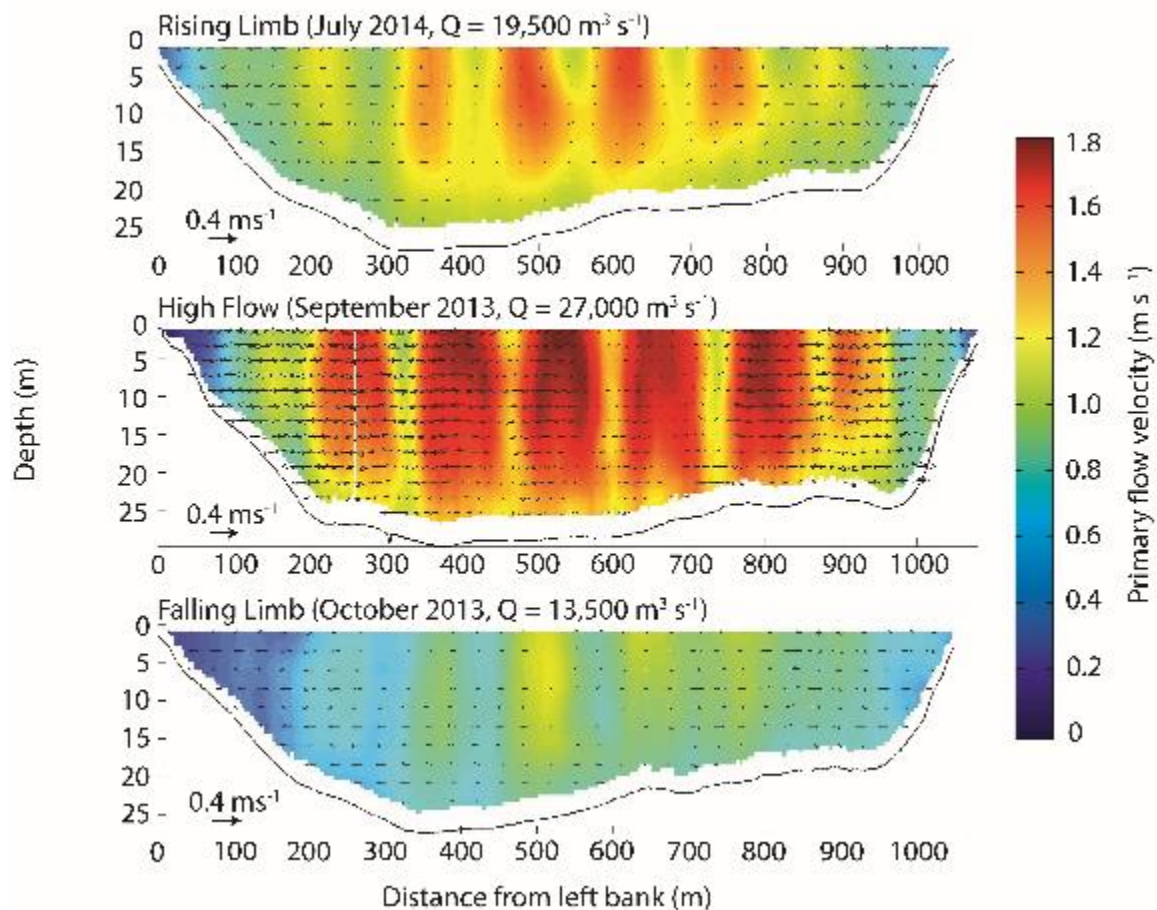
916 **Figure 1:** A) Landsat 8 image (October 2013) showing the island complex at Kampong  
 917 Cham with the location of the acoustic Doppler current profiler cross-sections (white  
 918 lines) and multi-beam echo sounder survey area (yellow checked box). The location  
 919 of the Kampong Cham gauge is shown by the white filled circle. B) Hydrograph from  
 920 Kampong Cham, Cambodia for 2013 and 2014 (solid lines) superimposed on the 1960  
 921 to 2002 mean annual hydrograph for the same station (dashed lines) with the timings  
 922 of the three surveys (yellow filled circles).





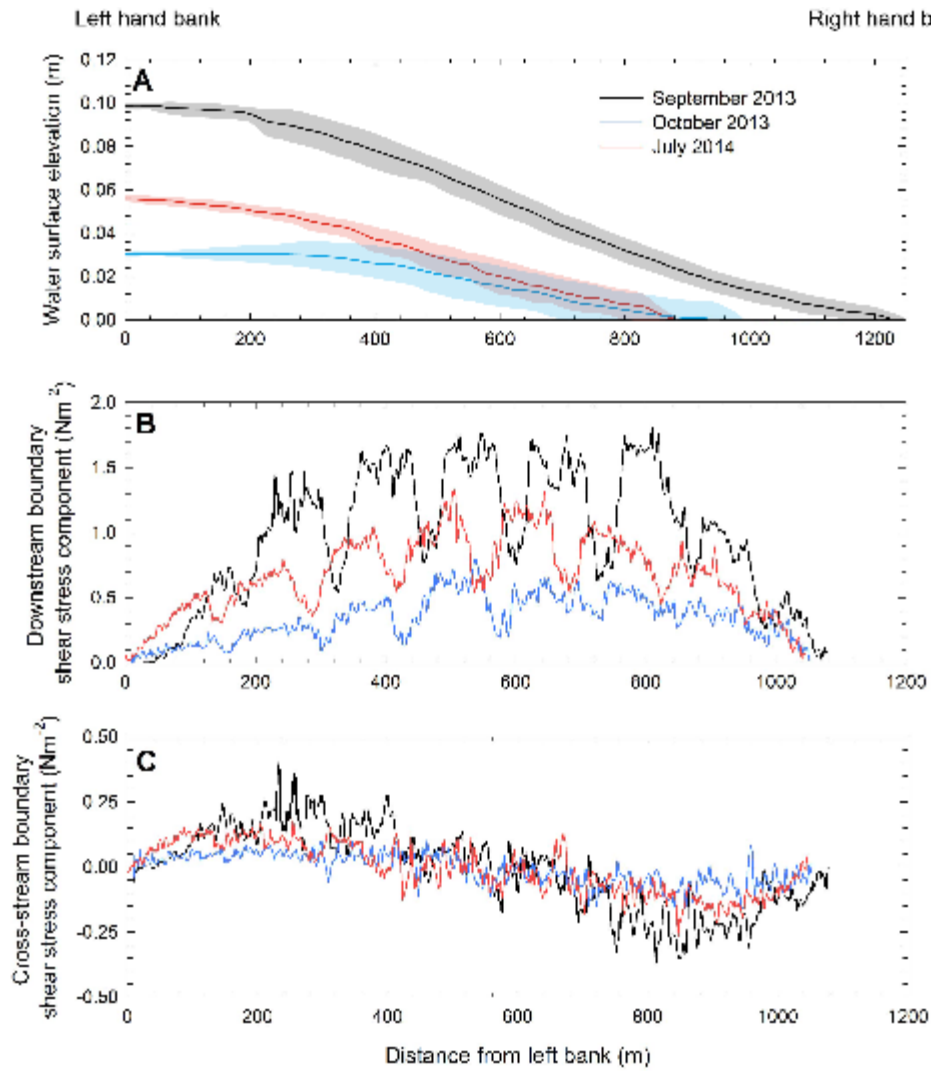
923

924 **Figure 2:** Relationships between corrected acoustic backscatter (dB) and measured  
 925 suspended sediment concentration ( $mg L^{-1}$ ) for the three aDcp units used in the study.  
 926 95% prediction bounds are shown in grey. For all fits,  $P < 0.05$ .



927

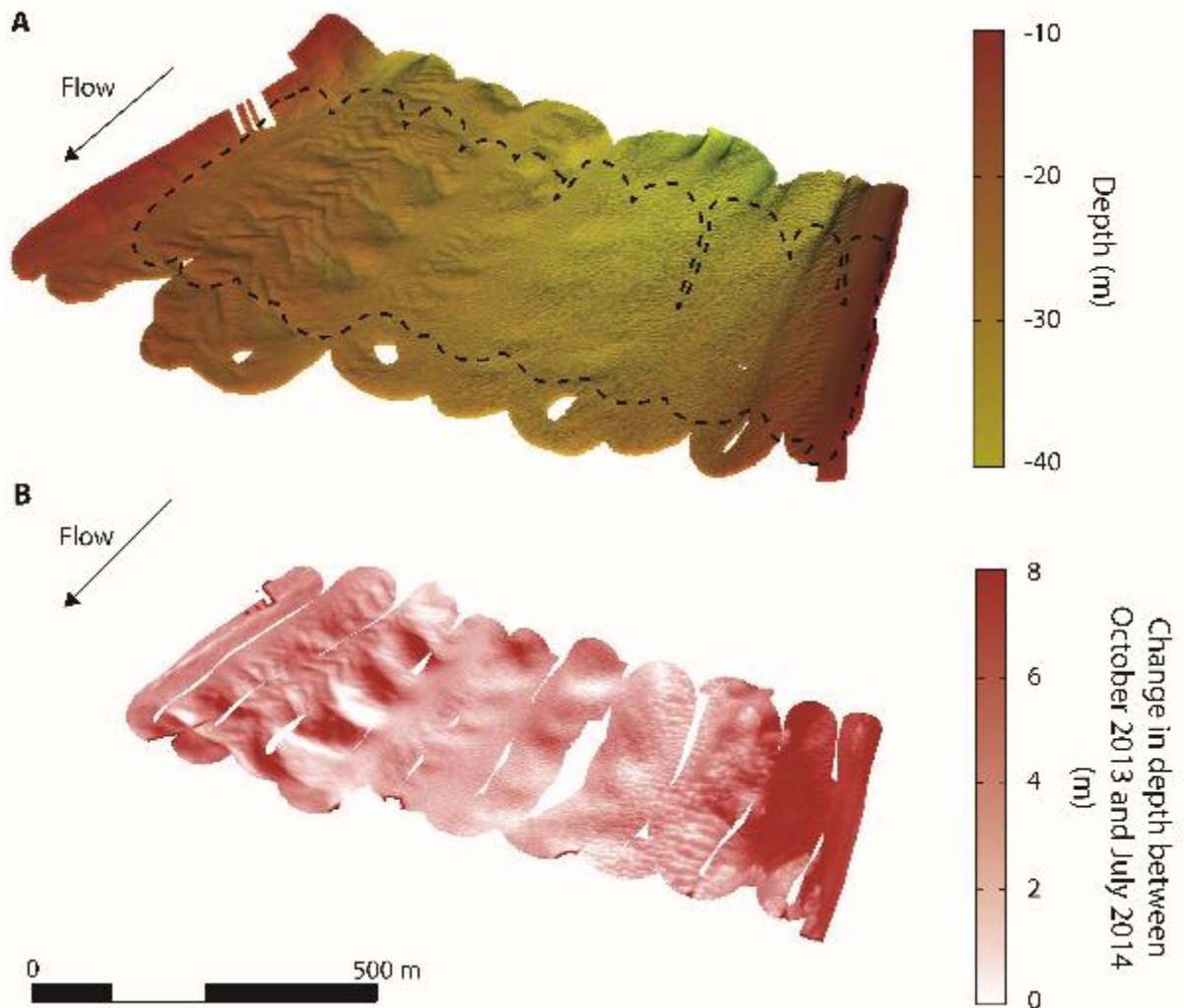
928 **Figure 3:** Primary flow velocities with secondary flow vectors for each of the three  
 929 surveys conducted at the bifurcation head (XS001; Figure 1A). Data were collected  
 930 using a 600 kHz aDcp. The vertical 'stripes' evident in the data represent the  
 931 presence of bridge piers located ~200 m upstream of the survey line.



932

933 **Figure 4: A)** Water surface elevations relative to the water elevation at the right hand  
 934 bank across the cross-section at the head of the bifurcation (XS001; Figure 1A) of  
 935 September 2013 ( $Q = 27,000 \text{ m}^3 \text{ s}^{-1}$ ; black line), October 2013 ( $Q = 13,500 \text{ m}^3 \text{ s}^{-1}$ ; blue  
 936 line) and July 2014 ( $Q = 19,500 \text{ m}^3 \text{ s}^{-1}$ ; red line). The data is derived from dGPS data  
 937 collected during the MBES surveys around the bifurcation head averaged at 2.5 m  
 938 intervals across the channel (cross-hatched box; Figure 1A). The shaded areas  
 939 represent 2 standard deviations in the average water surface elevation at each point  
 940 across the channel. **B)** The downstream component of the boundary shear stress as  
 941 derived from Eqs. 3-5 and flow velocity data from the aDcp transect at XS001. **C)** The  
 942 cross-stream component of the boundary shear stress as derived from Eqs 3-5 and

943 flow velocity data from the aDcp transect at XS001. Positive cross-stream shear  
944 stresses denote a vector towards the left hand bank, negative shear stresses denote  
945 a vector towards the right hand bank. The undulations in panels B) and C) are due to  
946 the location of the transect near bridge piers, and are reflected in the velocity profiles  
947 in Figure 3.

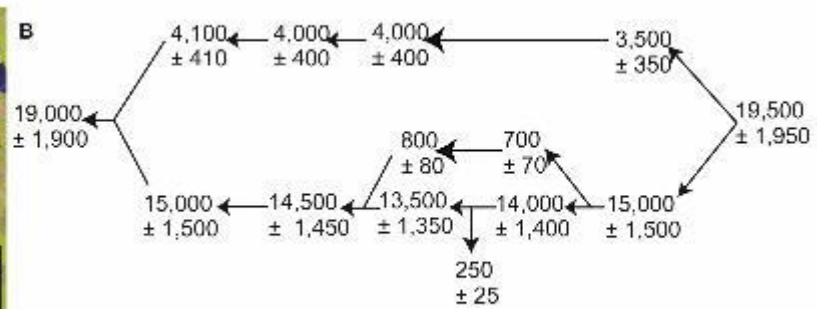


948

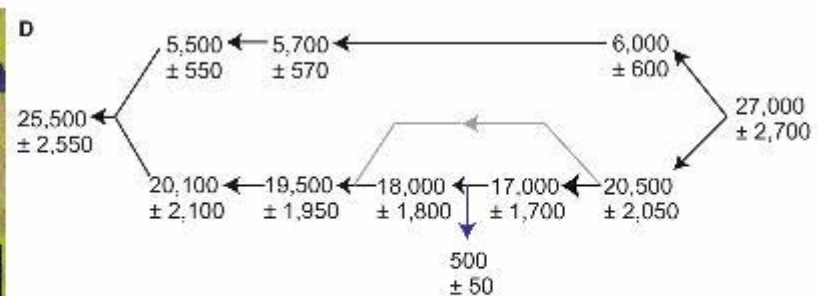
949 **Figure 5: A)** MultiBeam Echo Sounder bathymetry for October 2013. Dashed line  
950 represents area of repeat survey undertaken in July 2014. **B)** DEM of difference  
951 between July 2014 and October 2013. Scale bar applies to both panels. Flow is from  
952 top to bottom in each panel.



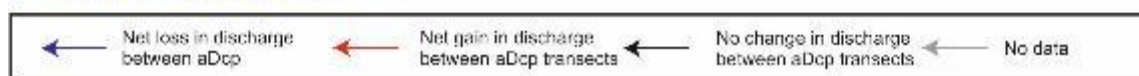
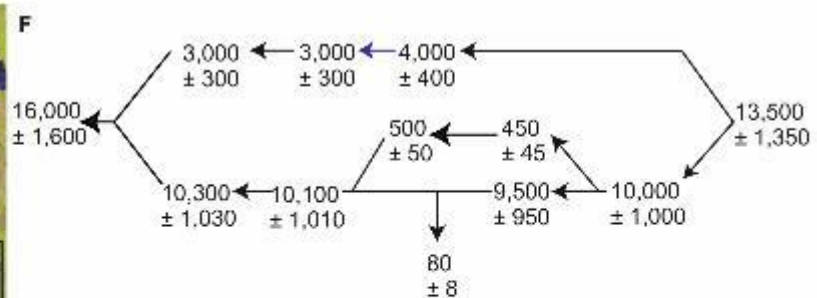
**Discharge ( $\text{m}^3 \text{s}^{-1}$ )  
Rising Limb (July 2014)**



**High Flow (September 2013)**



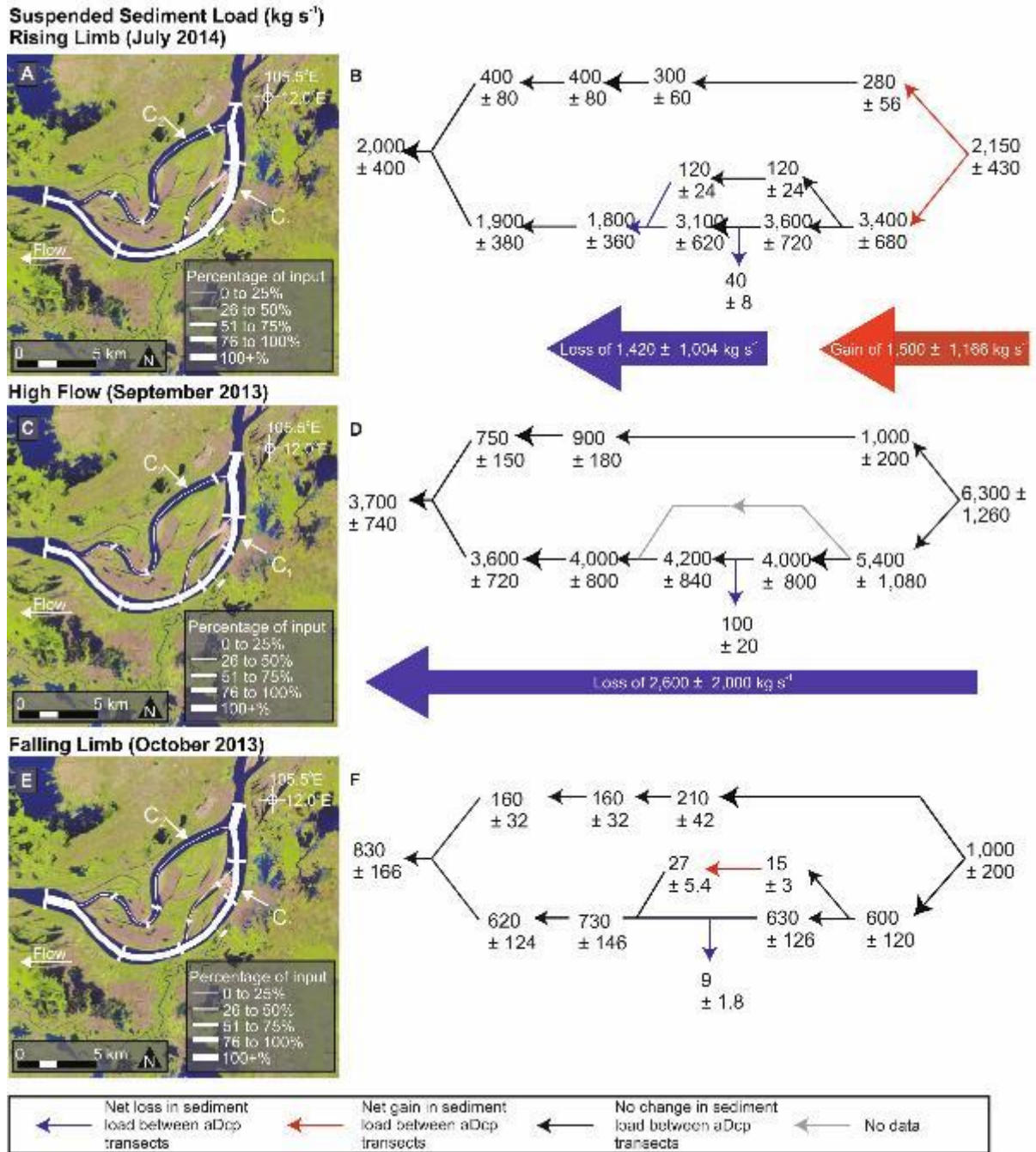
**Falling Limb (October 2013)**



953

954 **Figure 6:** Discharge ( $\text{m}^3 \text{s}^{-1}$ ) fluctuations through the difffluence-confluence unit. **A), C)**  
 955 **and E):** Flow diagrams with line widths proportional to the discharge measured at  
 956 XS001 (upstream extent) overlain on Landsat 8 imagery from October 2013. **B), D)**  
 957 **and F):** topological representations of discharge through the difffluence-confluence  
 958 unit on the rising limb, high flows and falling limbs, respectively. Links with gains (red),  
 959 losses (blue), no change (black) and no data (grey) are identified. Errors provided are

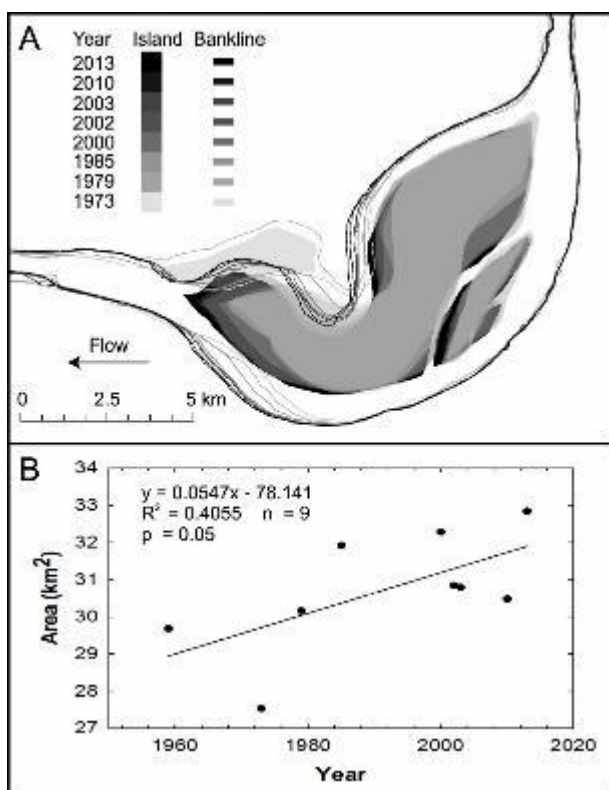
960 10% of the value, equivalent to one standard deviation of the repeat transects taken  
 961 at XS001. The large arrows beneath subplots B), D) and F) represent links with  
 962 significant gains (red) or losses (blue) where appropriate.



963

964 **Figure 7:** Suspended sediment load ( $\text{kg s}^{-1}$ ) fluctuations through the diffidence-  
 965 confluence unit. **A), C) and E):** Flow diagrams with line widths proportional to the  
 966 suspended sediment load measured at XS001 (upstream extent) overlain on Landsat

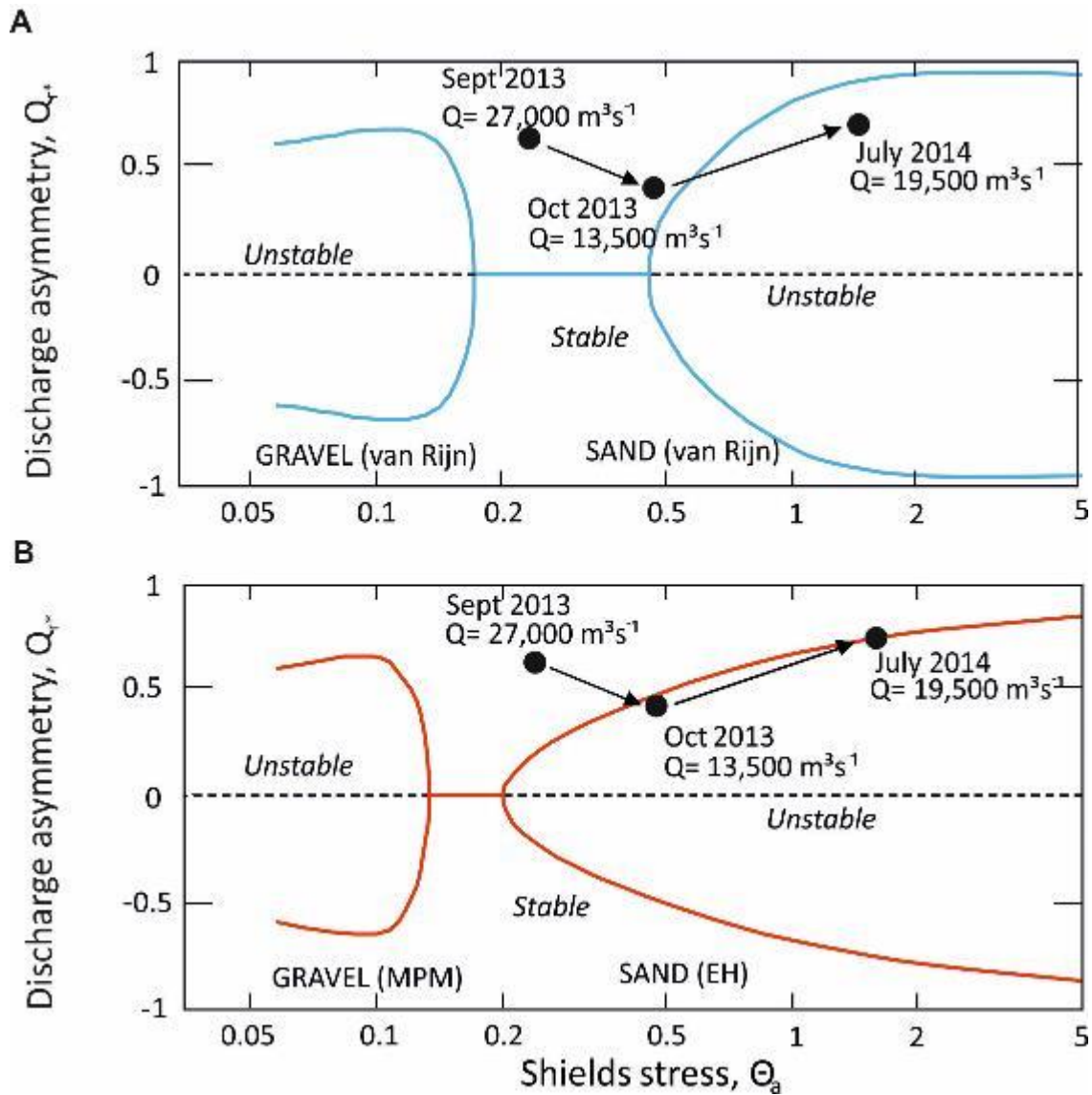
967 8 imagery from October 2013. **B), D) and F)**: topological representations of suspended  
968 sediment load through the diffluence-confluence unit on the rising limb, high flows and  
969 falling limbs, respectively. Links with gains (red), losses (blue), no change (black) and  
970 no data (grey) are identified. Errors provided are 20% of the value, equivalent to one  
971 standard deviation of the sediment load calculated from the repeat transects taken at  
972 XS001 (see text for details). The large arrows beneath subplots B), D) and F) represent  
973 links with significant gains (red) or losses (blue) where appropriate.



974

975 **Figure 8: A)** Island areal extents and banklines determined from Landsat imagery  
976 over the period 1959 – 2013. **B)** Total area covered by the island complex as a function  
977 of year calculated from the areas masked in the Landsat imagery depicted in panel A,  
978 showing average annual aggradation/progradation of 0.05 km<sup>2</sup> a year.





979

980 **Figure 9:** Equilibrium configurations of sand bed and gravel bed bifurcations from  
 981 Bolla-Pittaluga et al. (2015; modified from their figures 3a and b) for  $\beta_a = 50$  under **A)**  
 982 a suspended sediment dominant regime calculated using the van Rijn (1984)  
 983 formulation and **B)** a bedload sediment dominant regime calculated using the Meyer-  
 984 Peter and Müller (1948) and Engelund and Hansen (1967) formulations for gravel bed  
 985 and sand bed rivers, respectively. Calculated discharge asymmetry ratios and Shields  
 986 stresses for the three survey periods of the Mekong bifurcation are superimposed as  
 987 black filled circles with discharges labelled. The arrows depict the temporal trend in  
 988 the observed data.



